Resolvent-based modeling of turbulent jet noise

Ethan Pickering,[1, a)] Aaron Towne,[2, b] Peter Jordan,[3, c] and Tim Colonius[1, d]
[1] *Division of Engineering and Applied Science, California Institute of Technology, Pasadena, CA, 91125, USA*
[2] *University of Michigan, Ann Arbor, MI, USA*
[3] *Institut Pprime, CNRS / Université de Poitiers /ENSMA, 86962 Futuroscope Chasseneuil, France*

(Dated: 18 March 2021)

Resolvent analysis has demonstrated encouraging results for modeling coherent structures in jets when compared against their data-educed counterparts from high-fidelity large-eddy simulations (LES). We formulate resolvent analysis as an acoustic analogy that relates the near-field forcing to the near-field pressure field and the far-field acoustics. We use an LES database of round, isothermal, Mach 0.9 and 1.5 jets to produce an ensemble of realizations for the acoustic field that we project onto a limited set of resolvent modes. In the near-field, we perform projections on a restricted acoustic output domain, $r/D = [5, 6]$, while the far-field projections are performed on a Kirchhoff surface comprising a 100-diameter arc centered at the nozzle. This allows the LES realizations to be expressed in the resolvent basis via a data-deduced, low-rank, cross-spectral density matrix. We observe substantial improvements to the acoustic field reconstructions with the addition of a RANS-derived eddy-viscosity model to the resolvent operator and find that a single resolvent mode reconstructs the most energetic regions of the acoustic field across Strouhal numbers, $St = [0 - 1]$, and azimuthal wavenumbers, $m = [0, 2]$. Finally, we present a simple function that results in a rank-1 resolvent model agreeing within 2dB of the peak noise for both jets.

 [http://dx.doi.org(DOI number)]

[Submitted to J. Acoust. Soc. Am.] Pages: 1–18

I. INTRODUCTION

The goal of this work is to develop jet-noise models founded upon the physics of turbulent flows that are both low-rank and that provide insights into the mechanisms primarily responsible for noise generation. Resolvent analysis (McKeon and Sharma, 2010), also known as input-output analysis (Jovanović, 2021), provides a useful framework for achieving these goals. The central idea of the resolvent framework is similar to that of an acoustic analogy (Goldstein, 2003; Lighthill, 1952), whereby a forcing term, related to the statistics of the hydrodynamic near-field turbulence, gives rise, through a linear operator, to the observed far-field sound. The resolvent framework differs in two important ways. First, the operator is decomposed into its singular components that represent the maximal amplification between the forcing and the output. This permits the resulting acoustic field to be described at low rank, and thus limits the forcing statistics that must be modeled. Secondly, the full linearized Navier-Stokes equations are used as the propagator, and we seek a modal basis that represents *both* near and far-field coherent structures.

Before recent advances in computational power, the idea of modeling both the hydrodynamic component along with the acoustics would have been seen as both unnecessary and computationally taxing. However, the ability to resolve both components of the flow is in fact a benefit. Starting with the experimental findings of Mollo-Christensen (1967) and Crow and Champagne (1971), it has become clear that coherent structures in the hydrodynamic near-field are directly responsible for far-field sound (Jordan and Colonius, 2013). These structures take the spatio-temporal form of wavepackets and have been found to be the dominant source for aft-angle sound (Jordan and Colonius, 2013), as well as partial contributors to sideline noise (Jeun and Nichols, 2018; Papamoschou, 2018). These wavepackets may be linked to the early works of Crighton and Gaster (1976) (and Michalke (1977)) who hypothesized that coherent structures could be described as linear instability modes of the mean flow via modal analysis. However, it has now become apparent that the correct representation of wavepackets is that of a highly-amplified response to turbulent fluctuations, which is directly found via the resolvent framework.

Resolvent analysis uses the Singular Value Decomposition (SVD) to decompose the linear resolvent operator, identifying sets of orthogonal *forcing/input* and *response/output* modes, and ranking them in terms of the corresponding energetic gain between the forcing and response. This is particularly important as it allows our

[a] Postdoctoral Associate; epickeri@mit.edu
[b] Assistant Professor of Mechanical Engineering
[c] CNRS Research Director
[d] Frank and Ora Lee Marble Professor of Mechanical Engineering

model to self-select the most relevant amplification mechanisms for noise generation. This allows for a natural truncation of the resolvent basis that produces a reduced-order model, or in other words, a reduced-rank acoustic analogy.

Several studies have applied resolvent analysis to develop low-rank jet models (Cavalieri *et al.*, 2019; Jeun *et al.*, 2016; Lesshafft *et al.*, 2019). The existence of relatively low-rank responses in round, turbulent jets was shown by Schmidt *et al.* (2018), with significant agreement between structures found through spectral proper orthogonal decomposition (Towne *et al.*, 2018) (SPOD) of a high-fidelity experimentally-verified large-eddy simulations (LES) of jets (Brès *et al.*, 2017, 2018). Of particular relevance to this study are "acoustic resolvent modes" induced by performing resolvent analysis with an output domain defined over a region where fluctuations are purely acoustic. Through implementation of an acoustic output domain, resolvent analysis is able to filter out energetic, but acoustically irrelevant structures in the near-field. Jeun *et al.* (2016) performed such an analysis and found that for a Mach 1.5 jet, at Strouhal number $St = 0.33$ and azimuthal wavenumber $m = 0$, that the first resolvent mode reconstructs 57% of the acoustic energy, but through inclusion of the next 23 resolvent modes the reconstruction improved to 70% of the acoustic energy. This study looks to perform a similar analysis, in that we compute many acoustic resolvent modes and assess how well they reconstruct the acoustic energy. However, we also look to reduce the rank of the far-field significantly with the use of an eddy-viscosity model (Pickering *et al.*, 2020b) and generalize the performance of the resolvent framework across frequencies $St = 0 - 1$, azimuthal wavenumbers $m = [0 - 2]$, and for two turbulent jets at Mach numbers of 0.9 and 1.5.

For a resolvent jet model to fully reconstruct flow statistics, and in this case those of the acoustic field, a resolvent-based model must incorporate sub-optimal modes (Schmidt *et al.*, 2018) and correctly describe correlations (i.e. covariance) between modes inherent to turbulent flow (Towne *et al.*, 2020). These correlations are analogous to the concept of "jittering", used to describe temporal modulations of acoustic sources, that has been shown to be critical for accurately describing the acoustic field in turbulent jets (Cavalieri *et al.*, 2011). In our approach, such temporal modulations, or jittering, may be represented through second-order statistics via the statistical representation of the resolvent operator (Towne *et al.*, 2018)

$$\boldsymbol{S}_{yy} = \boldsymbol{R}\boldsymbol{S}_{ff}\boldsymbol{R}^{*}, \tag{1}$$

where $\boldsymbol{S}_{yy}$ and $\boldsymbol{S}_{ff}$ are the cross-spectral density tensors of the response and the forcing respectively and $\boldsymbol{R}$ is the resolvent operator. This equation shows that if the forcing CSD, describing spatial correlations, can be modeled (Towne *et al.*, 2017; Zare *et al.*, 2017), then the resolvent operator identically reconstructs the flow statistics, $\boldsymbol{S}_{yy}$. If the forcing were spatially uncorrelated, $\boldsymbol{S}_{ff} = \boldsymbol{\Lambda}$, where $\boldsymbol{\Lambda}$ is a diagonal matrix, then the eigenvectors of $\boldsymbol{S}_{yy}$, which are the SPOD modes of the outputs, are aligned with the eigenvectors of $\boldsymbol{R}\boldsymbol{R}^{*}$ (Towne *et al.*, 2018), or the response modes of the resolvent operator, $\boldsymbol{R}$. However, the uncorrelated condition is rarely met, resulting in discrepancies between resolvent and SPOD modes that must be resolved through modeling $\boldsymbol{S}_{ff}$.

One approach for modeling, at least partially, $\boldsymbol{S}_{ff}$ has been through the inclusion of a turbulence model to the resolvent operator. This approach has been implemented via an eddy-viscosity model in several flow configurations, from wall-bounded (Hwang and Cossu, 2010; Morra *et al.*, 2019) to free shear flows (Pickering *et al.*, 2020b). The latter study, quantifying the effect on turbulent jet modeling, found that the use of an eddy-viscosity model (utilizing only quantities available from RANS models) significantly improved the agreement between SPOD and resolvent modes, thus reducing the effort required to model the effective $\boldsymbol{S}_{ff}$ by diminishing the magnitude of the off-diagonal terms. We utilize the same eddy-viscosity model in the present work to better model the acoustic field.

This paper explores an approach to describe the coupling between resolvent modes that is necessary for reconstructing the acoustic field with a minimal set of resolvent modes. The coupling provides directional and energetic variability in acoustic radiation inherently important for noise prediction (Cavalieri *et al.*, 2011). Determination of the coupling between modes is performed by leveraging an ensemble of LES realizations which are projected on to a limited (i.e. low-rank) set of acoustic resolvent modes. From these projections we attain a (drastically) reduced-order cross-spectral density between the retained modes–a Hermitian, frequency-dependent matrix of size $n \times n$ that accurately represents the acoustic field.

Organization of the manuscript is as follows. We first briefly describe the LES databases used, the main details pertaining to resolvent analysis, and present the statistical description of the resolvent framework for reconstructing the acoustic field and estimating the reduced order covariance matrix in § II. In § III we present resolvent modes and LES reconstructions in the resolvent basis for one frequency-wavenumber pair for the Mach 1.5 jet before generalizing the approach to both jets over $St = [0, 1]$ and $m = [0, 2]$, and to both the near- and far-field acoustic regions. In the near-field section we compare the impact of including a RANS eddy-viscosity model to the resolvent operator and find it presents a significantly more efficient resolvent basis. We then present results for the far-field, along an arc at $100D$ from the nozzle, and show that reconstructions for both jets may be found using only the optimal resolvent mode. Finally, we conclude with a discussion on how the correct forcing coefficients may be estimated for a predictive jet noise model.

II. METHODS

A. Large Eddy Simulation database

The LES database and resolvent analysis are fully described in Schmidt *et al.* (2018) and Towne *et al.* (2018). Transonic (Mach 0.9) and supersonic (Mach 1.5) jets were computed using the flow solver "Charles"; details on numerical methods, meshing, and subgrid-models can be found in Brès *et al.* (2018) and Brès *et al.* (2017) along with validation cases conducted at PPRIME Institute, Poitiers, France for the Mach 0.9 jet (Brès *et al.*, 2018). The Mach 0.9 and 1.5 jets have Reynolds numbers of $Re_j = \rho_j U_j D/\mu_j = 1.01 \times 10^6$ and $Re_j = 1.76 \times 10^6$, respectively, where subscript j gives the value at the center of the jet, ρ is density, μ is viscosity, and M_j is the Mach number $M_j = U_j/c_j$, with c_j as the speed of sound at the nozzle centerline.

Throughout the manuscript, variables are nondimensionalized by the mean jet velocity U_j, jet diameter D, and pressure $\rho_j U_j^2$, with the resulting equation of state $p = \frac{\rho T}{\gamma M_j^2}$, with T denoting temperature and γ the ratio of specific heats. Frequencies are reported in Strouhal number, $St = fD/U_j$, where f is the frequency. The database consists of 10,000 snapshots separated by $\Delta t c_\infty/D = 0.2$ and 0.1 for the $M_j = 0.9$ and $M_j = 1.5$ jets, respectively, with c_∞ as the ambient speed of sound, and interpolated onto a structured cylindrical grid $x, r, \theta \in [0, 30] \times [0, 6] \times [0, 2\pi]$, where x, r, θ are streamwise, radial, and azimuthal coordinates, respectively. Variables are reported by the vector

$$\boldsymbol{q} = [\rho, u_x, u_r, u_\theta, T]^T, \tag{2}$$

where u_x, u_r, u_θ are the three cylindrical velocity components.

To generate an ensemble of flow realizations for computing statistical averages, the LES database of 10,000 snapshots is segmented into bins of 256 snapshots, with an overlap of 75%, and under the implementation of a Hamming window, resulting in 153 realizations of the flow. Each realization is then decomposed in the azimuthal direction and in time. The temporal decomposition provides a resolution of $St = 0.026$ and $St = 0.0217$ the $M_j = 1.5$ and $M_j = 0.9$ jets, respectively, and the azimuthal decomposition is valid up to $m = 68$, however, the acoustically relevant azimuthal wavenumbers are much smaller (Juve *et al.*, 1979) and only azimuthal wavenumbers $m = [0 - 2]$ are considered in this paper.

Considering the LES database only extends to $r/D = 6$, we implement a Kirchhoff surface (details provided in Appendix A), to the azimuthally and temporally transformed realizations of the flow. In doing so, we create an ensemble of far-field realizations located along an arc, with angle ϕ, of $100D$ from the nozzle at each frequency and azimuthal wavenumber. As done in Brès *et al.* (2017), and associated experiments (Schlinker *et al.*, 2009, 2008), we specifically compute the acoustics for the aft-angle sound from $\phi = 100 - 160$ and find our acoustic far-field is in close agreement (within 2dB) with the far-field computed via a Ffowcs Williams-Hawkings (FWH) surface in the LES calculation. Alternatively, we could have proceeded with the FWH data, however, doing so would provide an inconsistency between the LES and resolvent approach taken here for the near to far-field propagation. Additionally, propagating the LES realizations with a Kirchhoff surface allows for a continuous computation of the arc, while the far-field data from the LES is coarser, with data located 5° apart.

B. Resolvent analysis

For the round, statistically-stationary, turbulent jets considered in this manuscript, the compressible Navier-Stokes, energy, and continuity equations are linearized via a standard Reynolds decomposition and Fourier transformed both in time and azimuthally to the compact expression

$$(i\omega \mathbf{I} - \mathbf{A}_m)\boldsymbol{q}_{m,\omega} = \boldsymbol{L}_{m,\omega}\boldsymbol{q}_{m,\omega} = \boldsymbol{f}_{m,\omega}, \tag{3}$$

where $\boldsymbol{L}_{m,\omega}$ is the forward linear operator, $\boldsymbol{f}_{m,\omega}$ constitutes the nonlinear forcing in each variable, $\omega = 2\pi St$ is the frequency, and m is the azimuthal wavenumber. Mean-flow quantities used in the operator are derived from a RANS model, fitted closely to the LES mean flow. Although the mean flows are similar, the computation of a RANS model, using the standard $\kappa - \epsilon$ closure equations, also provides an eddy-viscosity field. With previous results of Pickering *et al.* (2019) and Pickering *et al.* (2020b) showing substantially improved agreement between SPOD and resolvent modes with the inclusion of an eddy-viscosity model, we incorporate the eddy-viscosity field from the RANS as $\mu_T = cC_\mu k^2/\epsilon$, where c and C_μ are scaling constants ($c = 0.2$, $C_\mu = 0.0623$ for the $M_j = 0.9$ and $C_\mu = 0.0554$ for $M_j = 1.5$ jet), k is the turbulent kinetic energy field, and ϵ is the turbulent dissipation field. The equations for the operator are provided in Appendix B.

Continuing with the derivation of the resolvent/input-output operator, we rewrite equation (3) by moving $\boldsymbol{L}_{m,\omega}$ to the right-hand side to give,

$$\boldsymbol{q}_{m,\omega} = \boldsymbol{L}_{m,\omega}^{-1}\boldsymbol{f}_{m,\omega} = \boldsymbol{R}_{m,\omega}\boldsymbol{f}_{m,\omega}, \tag{4}$$

where $\boldsymbol{R}_{m,\omega} = \boldsymbol{L}_{m,\omega}^{-1}$ is the standard resolvent operator. To then specify particular domains for both the response and forcing, we may write the above as

$$\boldsymbol{q}_{m,\omega} = \boldsymbol{R}_{m,\omega}\boldsymbol{B}\boldsymbol{f}_{m,\omega}, \tag{5}$$

and define the output variable

$$\boldsymbol{y}_{m,\omega} = \boldsymbol{C}\boldsymbol{q}_{m,\omega}, \tag{6}$$

where $\boldsymbol{B}$ and $\boldsymbol{C}$ are input and output matrices. Inserting equation (5) into equation (6) gives the input-output relationship,

$$\boldsymbol{y}_{m,\omega} = \boldsymbol{C}\boldsymbol{R}_{m,\omega}\boldsymbol{B}\boldsymbol{f}_{m,\omega} = \boldsymbol{H}_{m,\omega}\boldsymbol{f}_{m,\omega}, \tag{7}$$

where $\boldsymbol{H}_{m,\omega} = \boldsymbol{C}\boldsymbol{R}_{m,\omega}\boldsymbol{B}$ is the resolvent input-output operator from $\boldsymbol{f}_{m,\omega}$ to $\boldsymbol{y}_{m,\omega}$. Then by introducing the compressible energy norm of Chu (1965),

$$\begin{aligned}\langle \boldsymbol{q}_1, \boldsymbol{q}_2 \rangle_E \\ = \int\int\int \boldsymbol{q}_1^* \mathrm{diag}\left(\frac{\bar{T}}{\gamma\bar{\rho}M^2}, \bar{\rho}, \bar{\rho}, \bar{\rho}, \frac{\bar{\rho}}{\gamma(\gamma-1)\bar{T}M^2}\right)\boldsymbol{q}_2 r \mathrm{d}x\mathrm{d}r\mathrm{d}\theta \\ = \boldsymbol{q}_1^* \boldsymbol{W} \boldsymbol{q}_2, \end{aligned} \tag{8}$$

(where superscript $*$ denotes the complex conjugate transpose) via the matrix $\boldsymbol{W}$ to the forcing and response ($\boldsymbol{W}_f = \boldsymbol{W}_y = \boldsymbol{W}$) the weighted resolvent input-output operator, $\hat{\boldsymbol{H}}_{m,\omega}$ is obtained:

$$\hat{\boldsymbol{H}}_{m,\omega} = \boldsymbol{W}_y^{1/2} \boldsymbol{H}_{m,\omega} \boldsymbol{W}_f^{-1/2}. \tag{9}$$

Resolvent modes may then be found by taking the singular value decomposition of the weighted resolvent input-output operator giving

$$\hat{\boldsymbol{H}}_{m,\omega} = \hat{\boldsymbol{U}}_{m,\omega} \boldsymbol{\Sigma}_{m,\omega} \hat{\boldsymbol{V}}^*_{m,\omega}, \tag{10}$$

where the optimal response and forcing modes are contained in the columns of $\boldsymbol{U}_{m,\omega} = \boldsymbol{W}_y^{-1/2}\hat{\boldsymbol{U}}_{m,\omega}$, with $\boldsymbol{U}_{m,\omega} = [\boldsymbol{u}^1_{m,\omega}, \boldsymbol{u}^2_{m,\omega}, ..., \boldsymbol{u}^N_{m,\omega}]$, $\boldsymbol{V}_{m,\omega} = \boldsymbol{W}_f^{-1/2}\hat{\boldsymbol{V}}_{m,\omega}$, $\boldsymbol{V}_{m,\omega} = [\boldsymbol{v}^1_{m,\omega}, \boldsymbol{v}^2_{m,\omega}, ..., \boldsymbol{v}^N_{m,\omega}]$, and $\boldsymbol{\Sigma}_{m,\omega} = \mathrm{diag}(\sigma^1_{m,\omega}, \sigma^2_{m,\omega}, ..., \sigma^N_{m,\omega})$ are the optimal gains (Towne *et al.*, 2018). The unweighted resolvent input-output operator may then be recovered as:

$$\boldsymbol{H}_{m,\omega} = \boldsymbol{U}_{m,\omega} \boldsymbol{\Sigma}_{m,\omega} \boldsymbol{V}^*_{m,\omega} \boldsymbol{W}_f. \tag{11}$$

C. Near acoustic field output matrix

For analysis of the near-field acoustics, the output matrix $\boldsymbol{C}$ is chosen to only include pressure, $p' = \frac{\rho'\bar{T}+\bar{\rho}T'}{\gamma M_j^2}$, from $x/D = [0, 30]$, and $r/D = [5,20]$. Ideally, the LES domain would extend from $r/D = [5, 20]$ so that the LES could be directly projected onto the resolvent basis, however, the LES database (i.e. the saved data from the LES) only extends to $r/D = 6$. Although one could define an output matrix $\boldsymbol{C}$ that only includes that surface at $r/D = 6$, the resolvent modes may still contain hydrodynamic behavior (unless allowed to propagate further from the jet), thus we use the larger domain to ensure the modes are entirely acoustic. Using the larger domain presents a clear loss of orthogonality in the space represented by the LES domain, which is alleviated by truncating the modes to $r/D = [5, 6]$ (after computing the resolvent SVD) and implementing a Moore-Penrose inverse such that a least-squares fit of the LES in the resolvent basis can be performed. While previous studies have suggested the use of a filter based on the turbulent kinetic energy of the jet within the input matrix $\boldsymbol{B}$ (Towne *et al.*, 2017), we take $\boldsymbol{B}$ to be identity for both the near- and far-field analyses for the sake of generality.

D. Far-field output matrix

To define an input-output relationship from the near-field forcing to the far-field acoustics, we introduce a Kirchhoff surface, applied as a linear operator, derived in Appendix A. We define three radii: R as the radial coordinate of the near-field cylindrical surface, r as the coordinate pertaining to the far-field cylindrical surface, and ρ representing the distance from the nozzle in spherical coordinates (e.g. $\rho/D = 100$ for this study). As described in § II B, the input-output problem is defined as

$$\boldsymbol{q}_{m,\omega} = \boldsymbol{R}_{m,\omega}\boldsymbol{B}\boldsymbol{f}_{m,\omega}, \tag{12}$$

$$\boldsymbol{y}_{m,\omega} = \boldsymbol{C}_{R,\rho}\boldsymbol{q}_{m,\omega}, \tag{13}$$

where the output matrix $\boldsymbol{C}_{R,\rho}$ is the total Kirchhoff operator that maps the near-field cylindrical surface, R, to the far-field spherical surface, ρ. This operator is linearly composed of many Kirchhoff surfaces, $\boldsymbol{C}_{R,r}$, detailed next.

The cylindrical Kirchhoff operator is comprised of several linear operations to ensure accurate results and is defined as,

$$\boldsymbol{C}_{R,r} = \boldsymbol{D}^*\boldsymbol{H}_r\boldsymbol{D}\boldsymbol{P}\boldsymbol{T}\boldsymbol{N}\boldsymbol{C}_R, \tag{14}$$

where $\boldsymbol{C}_R$ is a surface selection matrix ($\in \mathbb{R}^{N_{\mathrm{surface}} \times 5N_rN_x}$), $\boldsymbol{N}$ is an interpolation matrix from a non-uniform grid to a uniform grid with $\Delta x/D = 0.025$ ($\in \mathbb{R}^{N_{\mathrm{uniform}} \times N_{\mathrm{surface}}}$), $\boldsymbol{T}$ is a Tukey windowing matrix (using a taper value of 0.75) that extends over the Kirchhoff surface to reduce spectral leakage ($\in \mathbb{R}^{N_{\mathrm{uniform}} \times N_{\mathrm{uniform}}}$), $\boldsymbol{P}$ is a padding matrix extending the uniform grid with a total of 2^n points (n is set to 15) for computing the upstream and downstream wave propagation, as well as ensuring sufficient accuracy in the transform of the initial surface ($\in \mathbb{R}^{2^n \times N_{\mathrm{uniform}}}$), $\boldsymbol{D}$ is the discrete Fourier transform (DFT) matrix ($\in \mathbb{R}^{2^n \times 2^n}$), and $\boldsymbol{H}$ contains the derived Hankel functions of the Kirchhoff surface, with entries along the diagonal for each azimuthal wavenumber, for a specified radial distance, r, from the surface at R ($\in \mathbb{R}^{2^n \times 2^n}$).

However, the above operator only supports one specified radial distance from the cylindrical surface at R, and a linear combination of $\boldsymbol{C}_{R,r}$ and a proper selection of streamwise points is required to construct a spherical arc. Thus, the linear expression to construct the total Kirchhoff operator is then

$$\boldsymbol{C}_{R,\rho} = \sum_{i=1}^{N_C} \boldsymbol{C}_{x_i}\boldsymbol{C}_{R,r_i}, \tag{15}$$

where x_i represents the streamwise location in the $100D$ arc and r_i represents the radial extent to which the Kirchhoff surface must propagate from surface R to the far-field arc ρ for the respective streamwise location. Points are defined along the arc from $\phi = 100° - 160°$ with a resolution of $\Delta\phi = 0.5°$.

E. Statistics

The statistics we are interested in are contained within the cross-spectral density (CSD) tensor, which

may be found for the desired output space by multiplying the resolvent equation by its complex conjugate transpose and taking the expectation (Towne *et al.*, 2018)

$$\langle \boldsymbol{y}_{m,\omega}\boldsymbol{y}^*_{m,\omega}\rangle = \langle \boldsymbol{H}_{m,\omega}\boldsymbol{f}_{m,\omega}\boldsymbol{f}^*_{m,\omega}\boldsymbol{H}^*_{m,\omega}\rangle, \tag{16}$$

giving

$$\boldsymbol{S}_{yy,m,\omega} = \boldsymbol{H}_{m,\omega}\boldsymbol{S}_{ff,m,\omega}\boldsymbol{H}^*_{m,\omega}, \tag{17}$$

where $\boldsymbol{S}_{yy,m,\omega}$ and $\boldsymbol{S}_{ff,m,\omega}$ are the CSD tensors of the response and the forcing, respectively. For brevity, we drop the subscripts m and ω and note that all CSD tensors and resolvent matrices must be defined for specific m and ω pairs in the remainder of the manuscript.

As mentioned earlier, this representation shows that if the forcing CSD tensor is known, then the resolvent operator reconstructs the response statistics. However, the forcing CSD is generally unknown. There are at least two potential avenues for modeling it. The first is to directly model $\boldsymbol{S}_{ff}$. To aid in such modeling efforts, $\boldsymbol{S}_{ff}$ may be computed directly from full LES data (Towne *et al.*, 2017), or estimated from limited flow statistics (Towne *et al.*, 2020). A second approach is to modify the resolvent operator by supplementing the governing linearized equations with an appropriately linearized turbulence model. In Pickering *et al.* (2020b), an eddy-viscosity model was considered and LES data was used to determine an optimal eddy viscosity field that would align, insofar as possible, the modes of $\boldsymbol{S}_{qq}$ (i.e. the full response statistics) with those of $\boldsymbol{R}\boldsymbol{R}^*$ (identical to $\boldsymbol{H}\boldsymbol{H}^*$ when $\boldsymbol{C} = \boldsymbol{B} = \boldsymbol{I}$). They found this to substantially reduce the magnitude of the off-diagonal terms of $\boldsymbol{S}_{ff}$, at least as the near-field coherent structures were concerned, consequently simplifying the number of terms that must be modeled.

In this study, we combine both modeling approaches. We first utilize the eddy-viscosity approximation of Pickering *et al.* (2020b) and then estimate a low-order approximation of the forcing CSD for the acoustic field. To do the latter, we return to equation (17) and expand the resolvent input-output operator through its singular value decomposition,

$$\boldsymbol{S}_{yy} = \boldsymbol{U}\boldsymbol{\Sigma}\boldsymbol{V}^*\boldsymbol{W}_f\boldsymbol{S}_{ff}\boldsymbol{W}_f\boldsymbol{V}\boldsymbol{\Sigma}\boldsymbol{U}^* \tag{18}$$

and define a covariance matrix $\boldsymbol{S}_{\beta\beta} = \boldsymbol{V}^*\boldsymbol{W}_f\boldsymbol{S}_{ff}\boldsymbol{W}_f\boldsymbol{V}$, where $\boldsymbol{\beta}$ is the projection of the forcing upon the resolvent input modes, $\boldsymbol{\beta} = \boldsymbol{V}^*\boldsymbol{W}_f\boldsymbol{f}$. This gives

$$\boldsymbol{S}_{yy} = \boldsymbol{U}\boldsymbol{\Sigma}\boldsymbol{S}_{\beta\beta}\boldsymbol{\Sigma}\boldsymbol{U}^* \tag{19}$$

which can be rearranged to solve for the covariance matrix,

$$\boldsymbol{S}_{\beta\beta} = \boldsymbol{\Sigma}^{-1}\boldsymbol{U}^*\boldsymbol{S}_{yy}\boldsymbol{U}\boldsymbol{\Sigma}^{-1}. \tag{20}$$

In its current state, the covariance matrix is exact, maintaining a full size of the system and permitting approximately 10^{11} degrees of freedom (i.e. $\boldsymbol{S}_{\beta\beta} \in \mathcal{C}^{5N_xN_r\times 5N_xN_r}$). To obtain a low-rank model of $\boldsymbol{S}_{\beta\beta}$ from the LES data, we compute $\boldsymbol{S}_{\beta\beta}$ with a truncated set of n resolvent modes, $\tilde{\boldsymbol{U}} \in \mathcal{C}^{5N_xN_r\times n}$, as,

$$\tilde{\boldsymbol{S}}_{\beta\beta} = \tilde{\boldsymbol{\Sigma}}^{-1}\tilde{\boldsymbol{U}}^*\boldsymbol{S}_{yy}\tilde{\boldsymbol{U}}\tilde{\boldsymbol{\Sigma}}^{-1}. \tag{21}$$

This reduces the size of the covariance matrix to $n\times n$, in that the degrees of freedom are now drastically reduced to $O(10^0 - 10^1)$.

With $\tilde{\boldsymbol{S}}_{\beta\beta}$, we may ask several questions: How well does $\tilde{\boldsymbol{S}}_{\beta\beta}$ reconstruct $\boldsymbol{S}_{yy}$ in the truncated resolvent basis? May $\tilde{\boldsymbol{S}}_{\beta\beta}$ be further reduced (e.g. neglect off-diagonal terms)? Can $\tilde{\boldsymbol{S}}_{\beta\beta}$ be modeled? For the latter two questions, we reserve discussion to § III D, where we both propose a forcing model and neglect the off-diagonal terms.

To address the former question, how well $\tilde{\boldsymbol{S}}_{\beta\beta}$ reconstructs $\boldsymbol{S}_{yy}$, the estimated response CSD is computed by

$$\tilde{\boldsymbol{S}}_{yy} = \tilde{\boldsymbol{U}}_y\tilde{\boldsymbol{\Sigma}}\tilde{\boldsymbol{S}}_{\beta\beta}\tilde{\boldsymbol{\Sigma}}\tilde{\boldsymbol{U}}^*_y. \tag{22}$$

The error between $\boldsymbol{S}_{yy}$ and $\tilde{\boldsymbol{S}}_{yy}$ may be assessed in a number of ways. For our purposes, the quantity of utmost importance is the power spectral density (PSD) of the acoustic field, which is located in the diagonal terms of $\boldsymbol{S}_{yy}$. When considering such comparisons at individual frequencies and azimuthal wavenumbers, a common comparison is through the difference in sound pressure level in decibels, dB, computed as

$$\Delta\mathrm{dB}(m, St) = 10\log\Big(\mathrm{diag}(\tilde{\boldsymbol{S}}_{yy} - \boldsymbol{S}_{yy})\Big). \tag{23}$$

This error metric is less than ideal when considering regions whose values vary by multiple orders of magnitude, such as noise levels between sideline and aft-angle regions. Given that our current approach uses an energy norm, the most energetic (i.e. loudest) regions are targeted and we present the raw PSD values (at each azimuthal wavenumber and frequency) rather than ΔdB for much of the results. To then consider the total noise levels in the acoustic field, we report the overall sounds pressure level (OASPL):

$$\mathrm{OASPL}(\phi) = 10\log_{10}\Bigg(\sum_{St_{\min}}^{St_{\max}} 2\sum_{-m_{\max}}^{m_{\max}} \mathrm{diag}(\boldsymbol{S}_{yy}(\phi, m, St))\Bigg). \tag{24}$$

Although this study focuses on the loudest regions, future iterations to our approach may use alternative norms, or output matrices, to optimally capture the sideline region. Such regions are also of importance as they are known to contain high-frequency noise, and consequently produce high effective perceived noise levels.

To provide further insight into the active physical mechanisms associated with the acoustic field (typically best described in the near-field), we use the original forcing modes computed from resolvent analysis and recalculate the responses with the response restriction matrix set to identity (i.e. $\boldsymbol{C} = \boldsymbol{I}$). This is computed as

$$\tilde{\boldsymbol{U}}_q = \boldsymbol{R}\tilde{\boldsymbol{V}}, \tag{25}$$

where $\tilde{\boldsymbol{U}}_q$ is the set of response modes of the full domain from the set of forcing modes $\tilde{\boldsymbol{V}}$ of the $\boldsymbol{C}_y$ restricted

domain. Although not performed in this study, one can in principle estimate the full state CSD,

$$\tilde{\boldsymbol{S}}_{qq} = \tilde{\boldsymbol{U}}_q \tilde{\boldsymbol{S}}_{\beta\beta} \tilde{\boldsymbol{U}}_q^*. \tag{26}$$

The above statistical relations are valid when $\boldsymbol{U}$ and $\boldsymbol{V}$ are orthogonal bases in the same space as $\boldsymbol{y}$ and $\boldsymbol{f}$, respectively. However, in the case of the near-field calculations, $\boldsymbol{U}$ is defined over a larger space than $\boldsymbol{y}$ and a pseudo inverse must be constructed to find the least-square solution to the above projections. First, we truncate the output modes $\boldsymbol{U}$ to the output space $x/D = [0, 30]$ and $r/D = [5,6]$ in the pressure field and define the associated output matrix as $\boldsymbol{C}_z$ where z denotes the new restricted space. Applying $\boldsymbol{C}_z$ to both the LES data and resolvent modes gives the ensemble of realizations $\boldsymbol{z}$ and resolvent modes $\boldsymbol{U}_z$. In addition to reducing the domain space, we also truncate the resolvent response basis to a limited set of n modes, as discussed above, represented as $\tilde{\boldsymbol{U}}_z$. There are now two important consequences of reducing the resolvent domain from $\boldsymbol{C}_y$ to $\boldsymbol{C}_z$. The first is a correction to the gain to the domain $\boldsymbol{C}_z$. Since both output domains share identical input modes we have,

$$\sigma_{i,y}^2 = \frac{\boldsymbol{u}_{i,y}^* \boldsymbol{W}_y \boldsymbol{u}_{i,y}}{\boldsymbol{v}_{i,f}^* \boldsymbol{W}_f \boldsymbol{v}_{i,f}}, \qquad \sigma_{i,z}^2 = \frac{\boldsymbol{u}_{i,z}^* \boldsymbol{W}_z \boldsymbol{u}_{i,z}}{\boldsymbol{v}_{i,f}^* \boldsymbol{W}_f \boldsymbol{v}_{i,f}}, \tag{27}$$

and the gain of the new domain is

$$\sigma_{i,z}^2 = \sigma_{i,y}^2 \frac{\boldsymbol{u}_{i,z} \boldsymbol{W}_z \boldsymbol{u}_{i,z}^*}{\boldsymbol{u}_{i,y}^* \boldsymbol{W}_y \boldsymbol{u}_{i,y}}], \tag{28}$$

where, by definition, $\boldsymbol{u}_{i,y}^* \boldsymbol{W}_y \boldsymbol{u}_{i,y} = 1$. The second is a loss of orthogonality. Fortunately, we may still determine a least squares fit of the data by computing the Moore-Penrose inverse of $\boldsymbol{W}_z^{1/2} \tilde{\boldsymbol{U}}_z$, $(\boldsymbol{W}_z^{1/2} \tilde{\boldsymbol{U}}_z)^+ = (\tilde{\boldsymbol{U}}_z^* \boldsymbol{W}_z \tilde{\boldsymbol{U}}_z)^{-1} \tilde{\boldsymbol{U}}_z^* \boldsymbol{W}_z^{1/2}$, and projecting it onto the CSD of z to estimate $\tilde{\boldsymbol{S}}_{\beta\beta}$

$$\tilde{\boldsymbol{S}}_{\beta\beta} = \tilde{\boldsymbol{\Sigma}}_z^{-1} (\boldsymbol{W}_z^{1/2} \tilde{\boldsymbol{U}}_z)^{+*} \boldsymbol{W}_z^{1/2} \boldsymbol{S}_{zz} \boldsymbol{W}_z^{1/2} (\boldsymbol{W}_z^{1/2} \tilde{\boldsymbol{U}}_z)^{+} \tilde{\boldsymbol{\Sigma}}_z^{-1}. \tag{29}$$

This approach is similar to the one taken by Towne *et al.* (2020) for assimilating partially observed flow statistics.

III. RESULTS

A. Near acoustic field

We begin by providing detailed results for a single frequency and azimuthal wavenumber pair of the $M_j = 1.5$ jet using the RANS eddy-viscosity resolvent operator. Figure 1 presents the first three resolvent modes computed with a restricted acoustic output domain ($r/D = [5, 20]$ in the fluctuating pressure field) and recast in the full domain by $\boldsymbol{U}_q = \boldsymbol{L}^{-1} \boldsymbol{V}_y$ for $M_j = 1.5$, $St = 0.26$, and $m = 0$. The associated gain of these modes, normalized by the first resolvent gain, are $[1, 0.17, 0.15]$ (and slowly decreasing with higher modes), indicating the first resolvent mode has at least six times the amplification to its associated forcing as the following resolvent modes.

The resolvent response modes show a particular pattern of acoustic beams. For the first mode there is a single, energetic acoustic beam, propagating at a shallow angle to the jet axis. The first suboptimal mode consists of two acoustic beams, similar to what was found by Jeun *et al.* (2016). This pattern is shown by the next suboptimal mode, with three beams located at the perimeter of the first suboptimal. Although not shown, this behavior continues for further suboptimal modes. Figure 2 compares three specific realizations of the $m = 0$, $St = 0.26$ field from the LES, $\boldsymbol{q}$, to the three-mode reconstructions of these fields found by projection, $\tilde{\boldsymbol{q}} = \tilde{\boldsymbol{U}}_q \tilde{\boldsymbol{\alpha}}$, where $\tilde{\boldsymbol{\alpha}} = \tilde{\boldsymbol{U}}_z^{+*} \boldsymbol{W}_z \boldsymbol{z}$. The three resolvent modes are able to accurately reconstruct the different radiation patterns evident in the realizations. Clearly there is constructive and destructive reinforcement amongst the three resolvent modes in order to produce the LES realizations.

For a quantitative assessment of the ability of the resolvent modes to reconstruct the acoustic field, we compute and compare the PSD pressure values by dB at $r/D = 6$ in figure 3. This is again performed for $St = 0.26$, $m = 0$, but now averaged over all $k = 153$ realizations. In addition to the three resolvent mode set, results are also shown for 5 and 10 mode sets. With just three modes we see that the peak directivity is well captured, with minor improvements (and diminishing returns) in the off-peak directivity with increasing numbers of modes.

We now extend our comparison to Strouhal numbers ranging from 0 to 1 and azimuthal wavenumbers 0-2 and assess the overall ability of the truncated resolvent basis to reconstruct the acoustic field. Figure 4 compares the PSD from the LES to its n-rank resolvent-basis reconstructions with $n = 1$, 3, 5, 10, and 20. The rank-1 model results are similar to those of Sinha et al. (Sinha *et al.*, 2014), who used parabolized stability equations and projected onto the first SPOD-mode at each $St - m$ pair. However, we show here that once additional modes are included, the reconstructions are substantially improved: the 20-mode model is indistinguishable from the LES for all frequencies and azimuthal modes, while even the 3-mode model is quantitatively accurate for $m = 0$ and $m = 1$.

Figure 5 is identical to Figure 4 but with data for the $M_j = 0.9$ jet. We see many similar behaviors to the $M_j = 1.5$ case, but it is apparent that a larger number of modes are required to reconstruct the near acoustic field. For example, about 10 modes are necessary to obtain a reasonable quantitative match (compared to just three modes at $M_j = 1.5$). This is consistent with multiple past observations where the $M_j = 0.9$ jet possesses non-negligible contributions from suboptimal modes that are correlated, or, as described in the time domain, as being linked via "jittering" (Cavalieri *et al.*, 2011), thus requiring many modes to reconstruct the acoustic field (Freund and Colonius, 2009; Towne *et al.*, 2015).

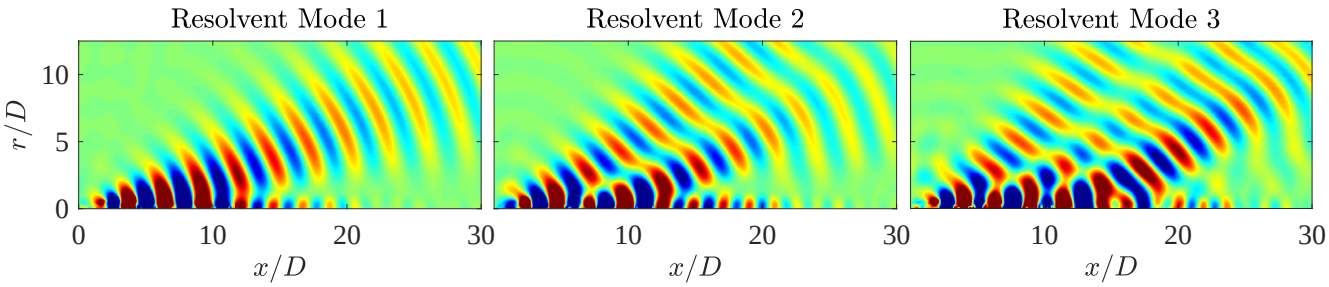

FIG. 1. The first three resolvent modes of fluctuating pressure, $q_{p'}$. Red and blue contours vary from ± 20% of the maximum fluctuating pressure of each mode, $\pm 0.2||q_{p'}||_\infty$. $M_j = 1.5$, $St = 0.26$, $m = 0$.

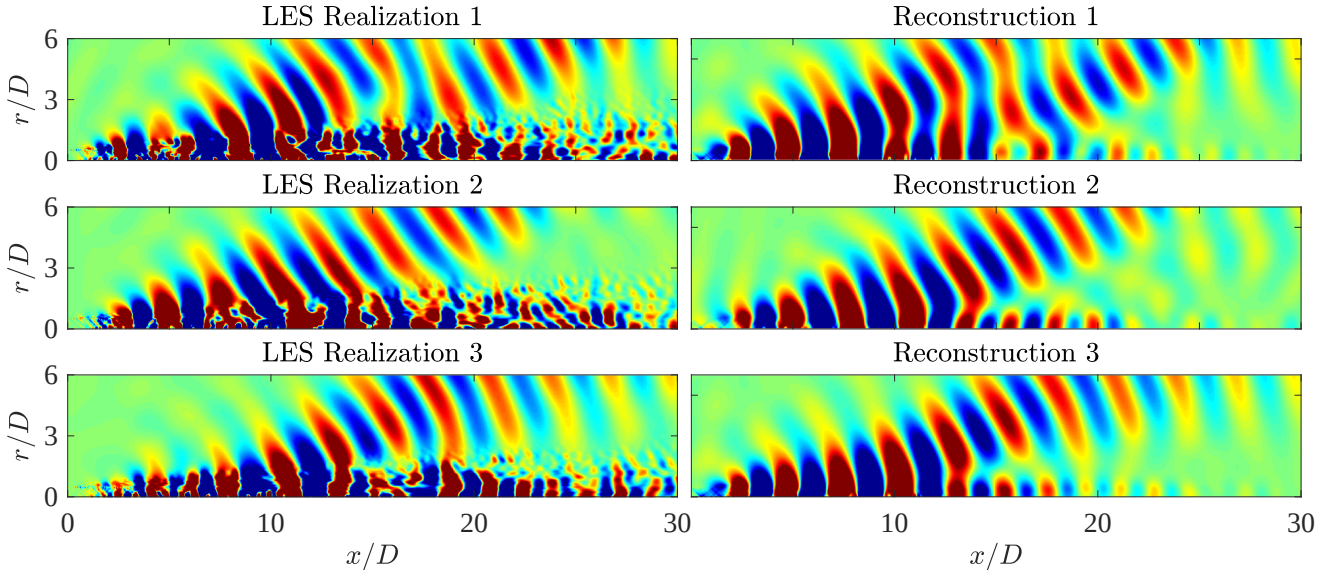

FIG. 2. Three LES realizations (left) and their associated three-mode resolvent reconstructions (right) of the pressure field at $M_j = 1.5$, $St = 0.26$, $m = 0$. Red and blue contours vary from ± 20% of the maximum fluctuating pressure of each LES realization, $\pm 0.2||q_{p'}||_\infty$.

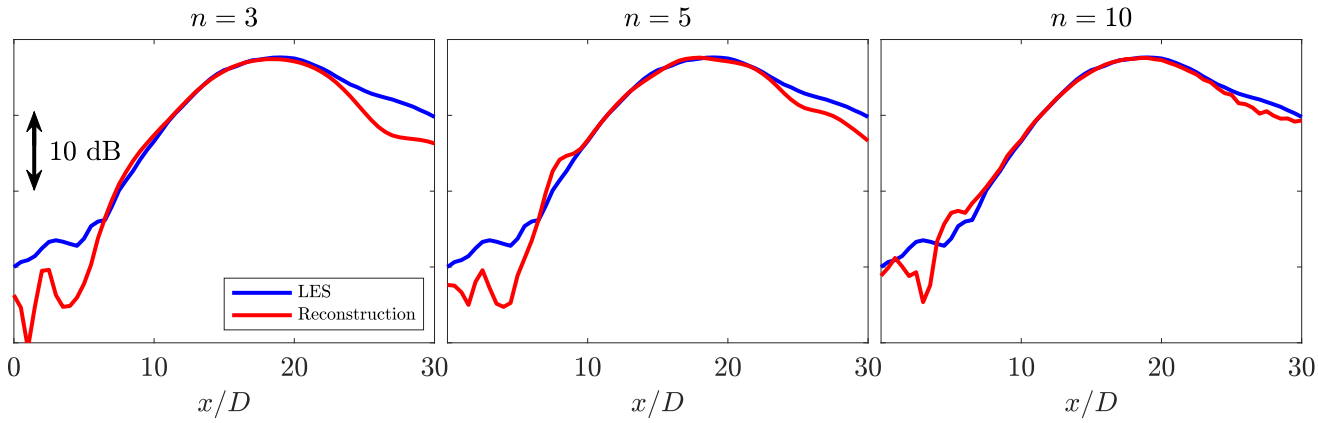

FIG. 3. Comparison of pressure PSD values by dB at $r/D = 6$ for the LES ensemble and reconstructions in the resolvent basis using 3, 5, and 10 resolvent modes.

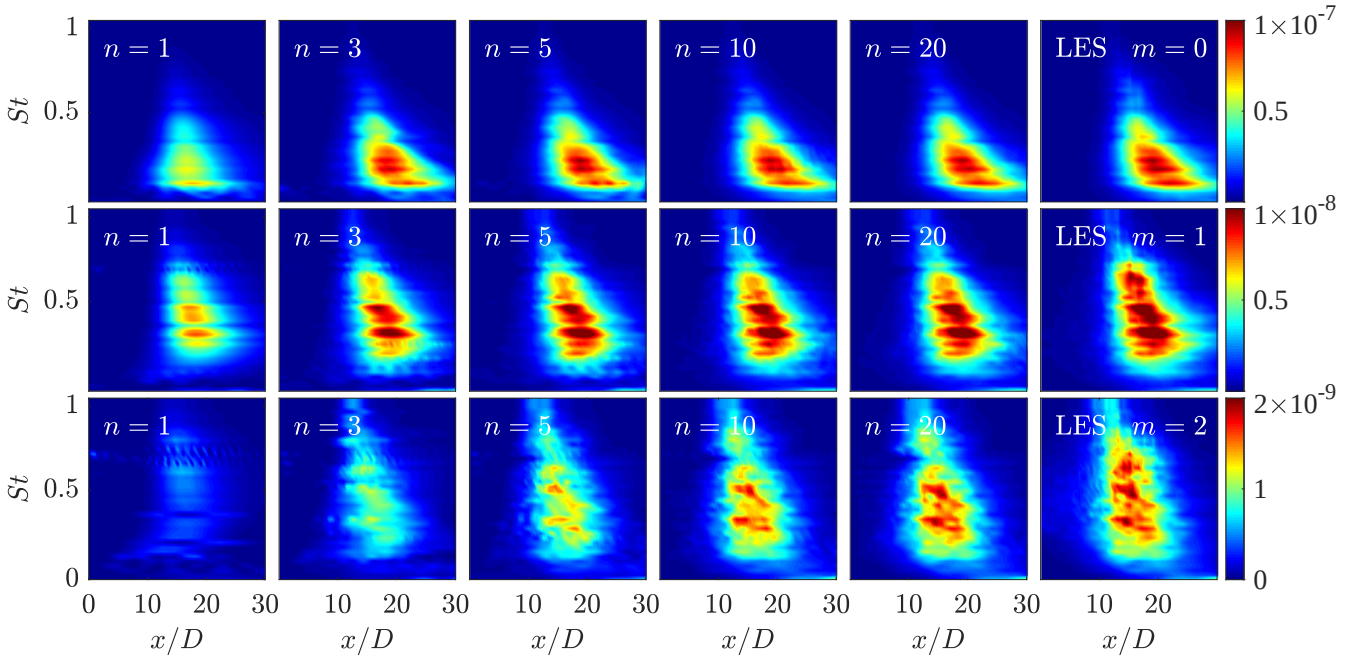

FIG. 4. PSD of resolvent reconstructions of the $M_j = 1.5$ jet with a RANS eddy-viscosity model at radial surface $r/D = 6$ from $St = [0, 1]$ and $x/D = [0, 30]$ for three azimuthal wavenumbers, $m = [0, 2]$, from top to bottom and using $n = 1, 3, 5, 10, 20$ modes from left to right. The right most column presents the LES values and the contour levels associated with each row.

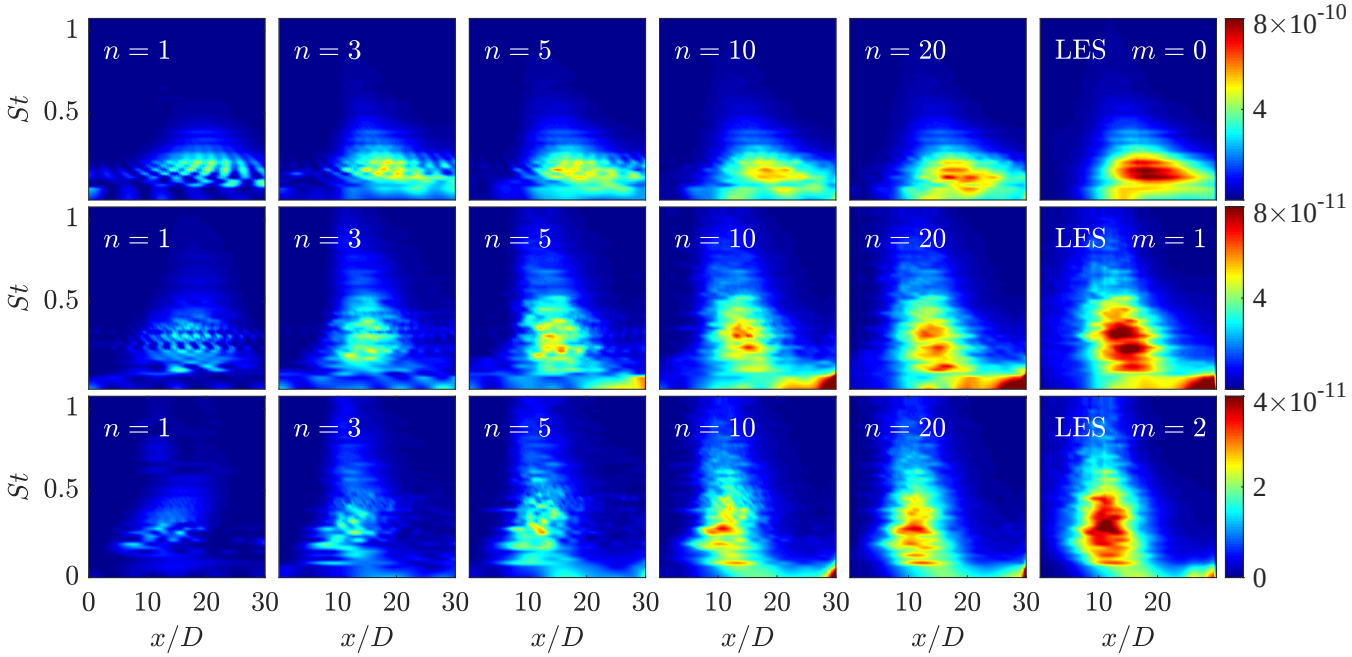

FIG. 5. PSD of resolvent reconstructions of the $M_j = 0.9$ jet with a RANS eddy-viscosity model at radial surface $r/D = 6$ from $St = [0, 1]$ and $x/D = [0, 30]$ for three azimuthal wavenumbers, $m = [0, 2]$, from top to bottom and using $n = 1, 3, 5, 10, 20$ modes from left to right. The right most column presents the LES values and the contour levels associated with each row.

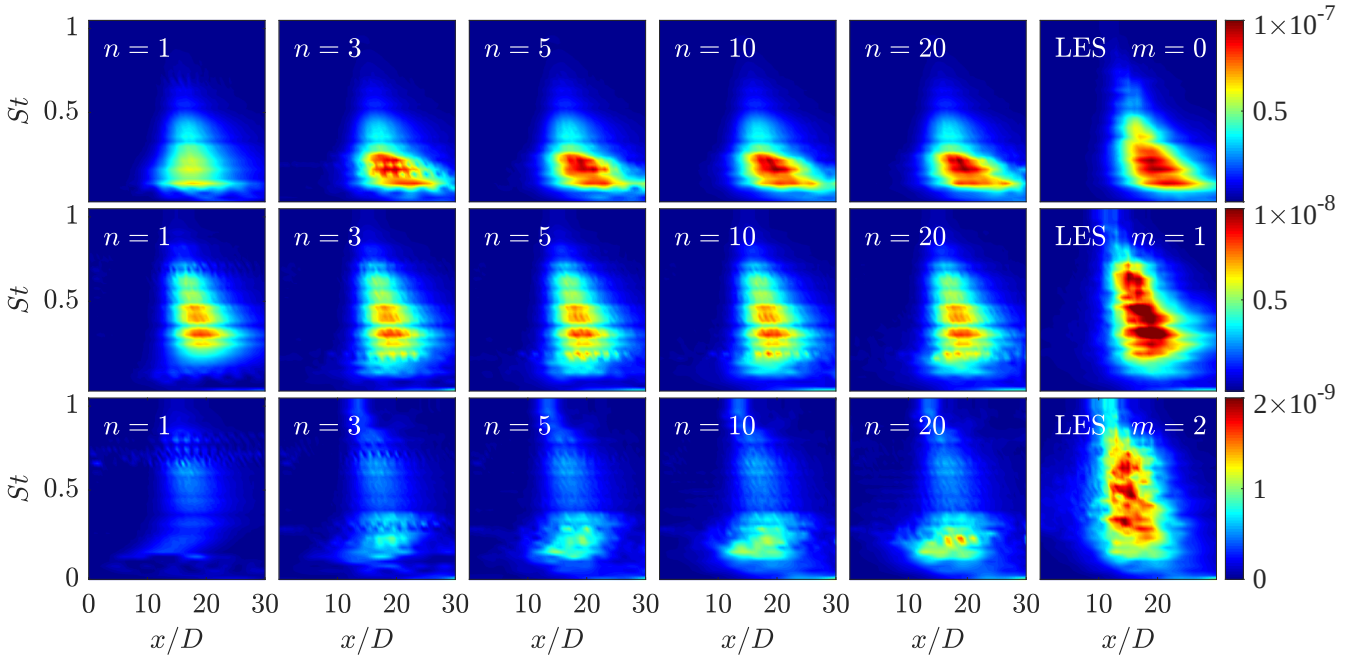

FIG. 6. PSD of resolvent reconstructions of the $M_j = 1.5$ jet *without* an eddy-viscosity model at radial surface $r/D = 6$ from $St = [0, 1]$ and $x/D = [0, 30]$ for three azimuthal wavenumbers, $m = [0, 2]$, from top to bottom and using $n = 1, 3, 5, 10, 20$ modes from left to right. The right most column presents the LES values and the contour levels associated with each row.

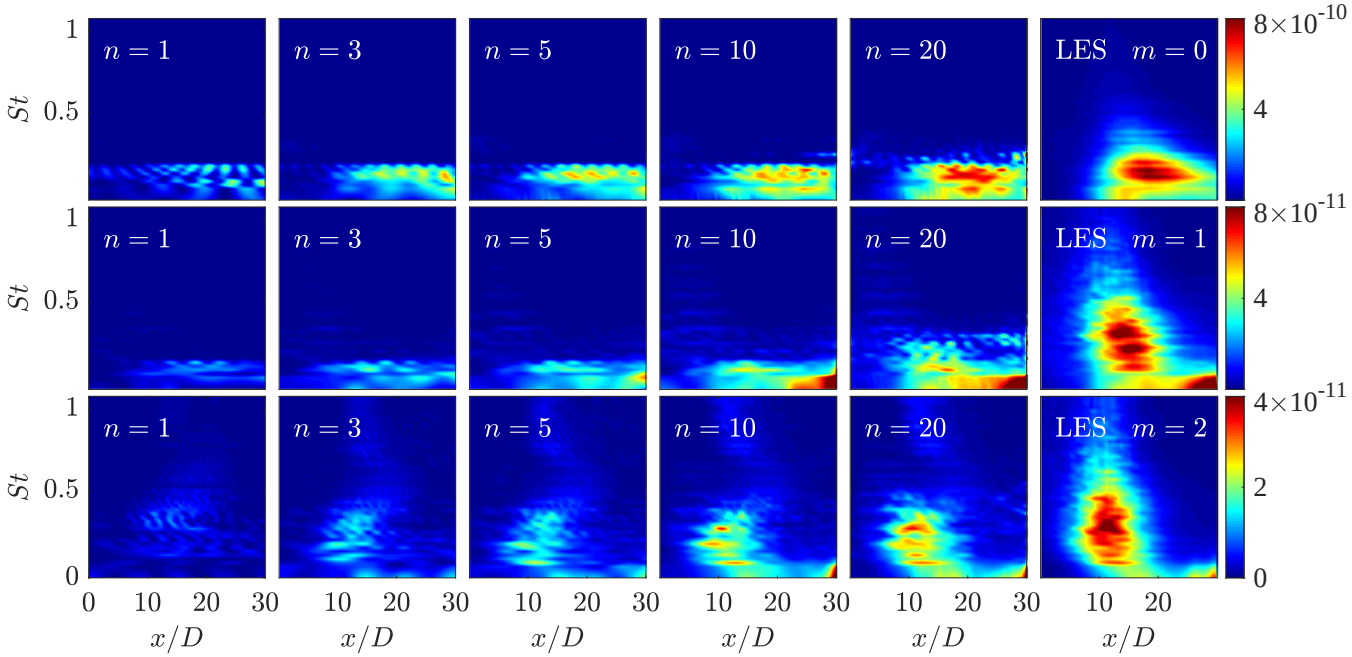

FIG. 7. PSD of resolvent reconstructions of the $M_j = 0.9$ jet *without* an eddy-viscosity model at radial surface $r/D = 6$ from $St = [0, 1]$ and $x/D = [0, 30]$ for three azimuthal wavenumbers, $m = [0, 2]$, from top to bottom and using $n = 1, 3, 5, 10, 20$ modes from left to right. The right most column presents the LES values and the contour levels associated with each row.

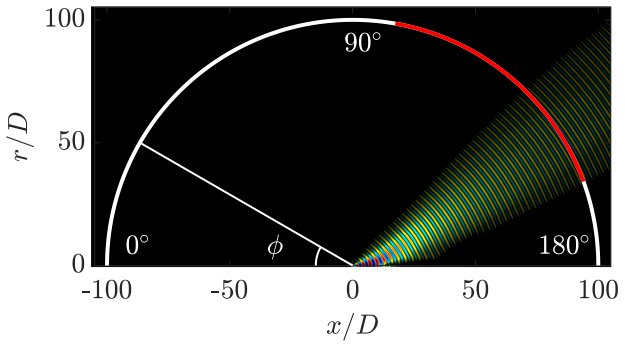

FIG. 8. Schematic of the far-field arc at $100D$ from the nozzle exit. The angle along the arc is defined as ϕ, with 0° on the upstream axis and 180° on the downstream axis. The red portion of the arc denotes the region of interest, $\phi = 100^\circ - 160^\circ$ and the acoustic beam presented is the first resolvent mode for $M_j = 1.5$, $St = 0.26$, $m = 0$, found for the far-field region.

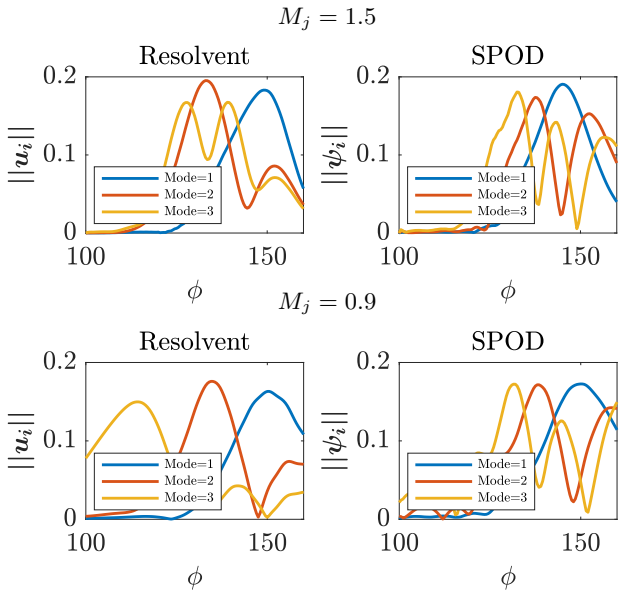

FIG. 9. Magnitude of the first three resolvent (left) and SPOD (right) modes computed on the far-field arc for the $M_j = 1.5$ (top) and $M_j = 0.9$ (bottom) jet at $St = 0.26$ and $m = 0$.

B. Utility of the eddy-viscosity model

The eddy-viscosity amended resolvent model used here was previously evaluated in terms of its ability to reconstruct the dominant near-field hydrodynamic SPOD modes (Pickering *et al.*, 2020b). In this section, we further demonstrate its utility in modeling the acoustic field. In figures 6 and 7, we plot PSD reconstructions similar to figures 5 and 4, respectively, but where the eddy viscosity model is switched off and a constant turbulent Reynolds number $Re_T = 3 \times 10^4$ is used instead. While the rank-1 models for the $M_j = 1.5$ jet are similar with and without the eddy viscosity, the remaining reconstructions show a strong and clear advantage to the adopted eddy-viscosity approach. Particularly as sub-optimal modes are added to the basis, the eddy-viscosity model converges rapidly toward the LES whereas the turbulent-Reynolds-number model shows little improvement. This result is consistent with our previous findings (Pickering *et al.*, 2020b), which showed a more profound effect of the eddy viscosity on sub-optimal modes associated with the Orr-mechanism than on modes associated with the Kelvin-Helmholtz mechanism, where the latter are dominant over most of the frequency-wavenumber space being considered here.

C. Far-Field Results

We now extend the eddy-viscosity enhanced resolvent basis to the far-field, and aim to find the modes that are optimal on an arc $100D$ from the nozzle and a range of polar angles from $\phi = 100^\circ$ to $\phi = 180^\circ$ (where $\phi = 180^\circ$ lies on the downstream axis). The domain is depicted in figure 8.

Figure 9 presents the magnitude of the first three resolvent modes along the arc for both jets at $St = 0.26$ and $m = 0$. The same three-beam structure apparent in figure 1 is evident here, with the dominant one-beam mode peaking at $\phi \approx 150^\circ$. This progression in beam number and location continues in the higher mode numbers not visualized here. One notable difference between the $M_j = 1.5$ and $M_j = 0.9$ jets is the width and spacing of the beams, with the $M = 0.9$ jet being more directive. Also plotted in figure 9 are the magnitude of modes found via spectral proper orthogonal decomposition (SPOD) of the LES data. These modes, which optimally reconstruct the CSD of the far-field arc, are useful to compare to the resolvent modes since a close correspondence between resolvent and SPOD modes indicates that the resolvent mode forcings are mutually uncorrelated (Towne *et al.*, 2018). Indeed, we see a reasonable agreement between the far-field SPOD and resolvent modes, with the single exception of mode three for the $M_j = 0.9$ jet. The amplitudes and exact locations vary slightly, but such close agreement suggests that an uncorrelated model may suffice.

Figure 10 shows the near-field signatures of the dominant three far-field modes plotted in figure 9 for the $M_j = 1.5$ jet. This plot should be directly compared to figure 1, which showed the dominant three near-field modes. Outside the jet, the modes are nearly indistinguishable. Within the jet (along the x-axis), there are differences that can be associated with the larger hydrodynamic wavepacket imprint left in the near-field modes and missing in the far-field ones.

We now assess how well the computed resolvent modes reconstruct the PSD of the far-field region across $St \in [0.1, 1]$ and $m = [0, 1, 2]$. Figures 11 and 12 compare $n = 1$, 2, 3, and 5-mode reconstructions to the LES PSD for the $M_j = 1.5$ and $M_j = 0.9$ jets, respectively. These plots are analogous to figures 4 and 5 except that the far-

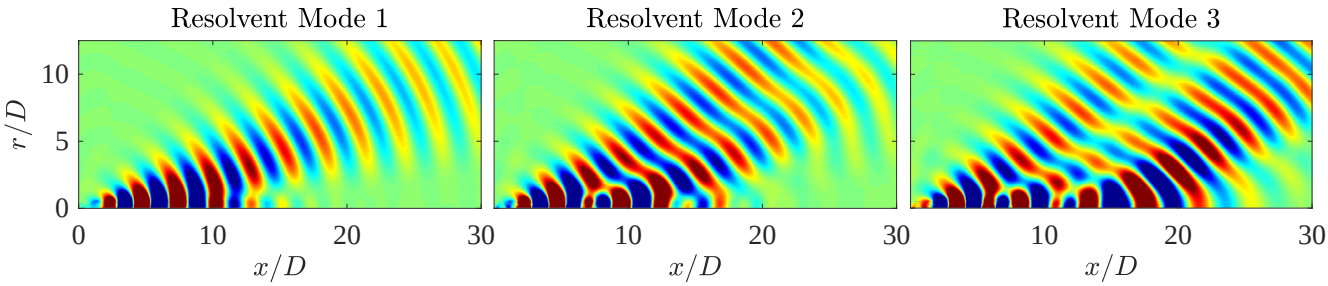

FIG. 10. The near-field of three resolvent modes of fluctuating pressure, $q_{p'}$, computed considering the $100D$ arc from $\phi = 100^\circ - 160^\circ$. Red and blue contours vary from $\pm$ 20% of the maximum fluctuating pressure of each mode, $\pm 0.2||q_{p'}||_\infty$. $M_j = 1.5$, $St = 0.26$, $m = 0$.

field modes are used and we concentrate on lower-rank reconstructions.

Looking first at the LES PSD for the $M_j = 1.5$ jet (figure 11), we see that when plotted against polar angle the distribution of PSD is similar to that plotted against x/D at $r/D = 6$, but the magnitude of the PSD has dropped by about an order of magnitude after propagating for $100D$. The $m = 0$ and $m = 1$ azimuthal wavenumbers are very directive over a narrow range of angles from $\phi = [140 - 155]$; $m = 2$ less so. The $m = 0$ azimuthal wavenumber has an amplitude that is about 10 and 100 times larger than the contour levels of $m = 1$ and $m = 2$, respectively, but is more concentrated at lower frequencies $St < 0.5$ whereas other azimuthal wavenumbers have similar energy over $0.5 < St < 1$.

Looking to the reconstructions at $M_j = 1.5$, we see that the the rank-1 resolvent reconstruction provides substantial agreement between the LES, fitting all of the loudest features. Increasing the rank captures nearly all the energy for each of the azimuthal wavenumbers; however, the increase in agreement with rank is rather gradual and serves largely to reconcile the quieter regions of the flow.

Turning to the $M_j = 0.9$ jet (figure 12), we see differences with the $M_j = 1.5$ case similar to those discussed in the previous section. Particularly, the $m = 1$ and $m = 2$ azimuthal wavenumbers are much less directive. Similar to the $M_j = 1.5$ jet, the $m = 0$ component is the loudest, about 30-fold compared to the $m = 1$ case and two orders of magnitude when compared to $m = 2$. Likewise, the $m = 0$ azimuthal wavenumber is most concentrated at $St < 0.5$. The reconstructions, however, are quite distinct from those at $M_j = 1.5$. While the $m = 0$ azimuthal wavenumber is relatively well captured at rank 1, with only negligible contributions from suboptimal modes, the $m = 1$ and $m = 2$ azimuthal wavenumbers are poorly reconstructed with one mode and show only modest convergence toward the full LES PSD up to $n = 5$. This higher-rank behavior is similar to what was observed when reconstructing with near-acoustic-field modes in the previous section.

D. A simple fit/model

Considering we may reconstruct the far-field acoustics at low-rank, we now ask whether we can define a simple forcing model. One approach would be to propose a form of the forcing cross-spectral density tensor, $\boldsymbol{S}_{ff}$, and project this form onto the resolvent input modes to produce a reduced-order matrix $\tilde{\boldsymbol{S}}_{\beta\beta}$. Despite some clear trends for the dependence of $\boldsymbol{S}_{ff}$ on mean flow quantities (Towne *et al.*, 2017), there does not yet exist a general form for estimating $\boldsymbol{S}_{ff}$. We investigate here an alternative approach of directly estimating $\tilde{\boldsymbol{S}}_{\beta\beta}$. That is, we focus on modeling the expansion coefficients rather than the forcing itself.

The estimated covariance matrix $\tilde{\boldsymbol{S}}_{\beta\beta}$ presents the least square reconstruction of the observed data and contains both the amplitudes and correlations necessary to force each resolvent mode. Where the forcings are uncorrelated, the estimated $\tilde{\boldsymbol{S}}_{\beta\beta}$ matrix becomes diagonal and only n coefficients (albeit at each azimuthal wavenumber and frequency) require modeling. However, even if the forcing is uncorrelated, minor errors or discrepancies in the data, data-processing, computation of resolvent mode, etc., result in a full $\tilde{\boldsymbol{S}}_{\beta\beta}$ matrix. Further, as rank increases, the statistical uncertainty in the terms becomes greater, reducing our hope for successful modeling. Thus, we explore whether neglecting off-diagonal terms is sufficient for a model, but note that this approach provides no guarantees for success; precisely stated, the approximation is not guaranteed to converge as the number of retained modes is increased (Towne *et al.*, 2018).

To limit uncertainty and prevent over-fitting, we assume that the forcing is uncorrelated (i.e. diagonal) and that the projection of the data with the first resolvent mode,

$$\tilde{\boldsymbol{S}}_{\beta\beta} = \boldsymbol{\Sigma}_1^{-1}\boldsymbol{U}_1^*\boldsymbol{S}_{yy}\boldsymbol{U}_1\boldsymbol{\Sigma}_1^{-1} = \lambda_\beta, \tag{30}$$

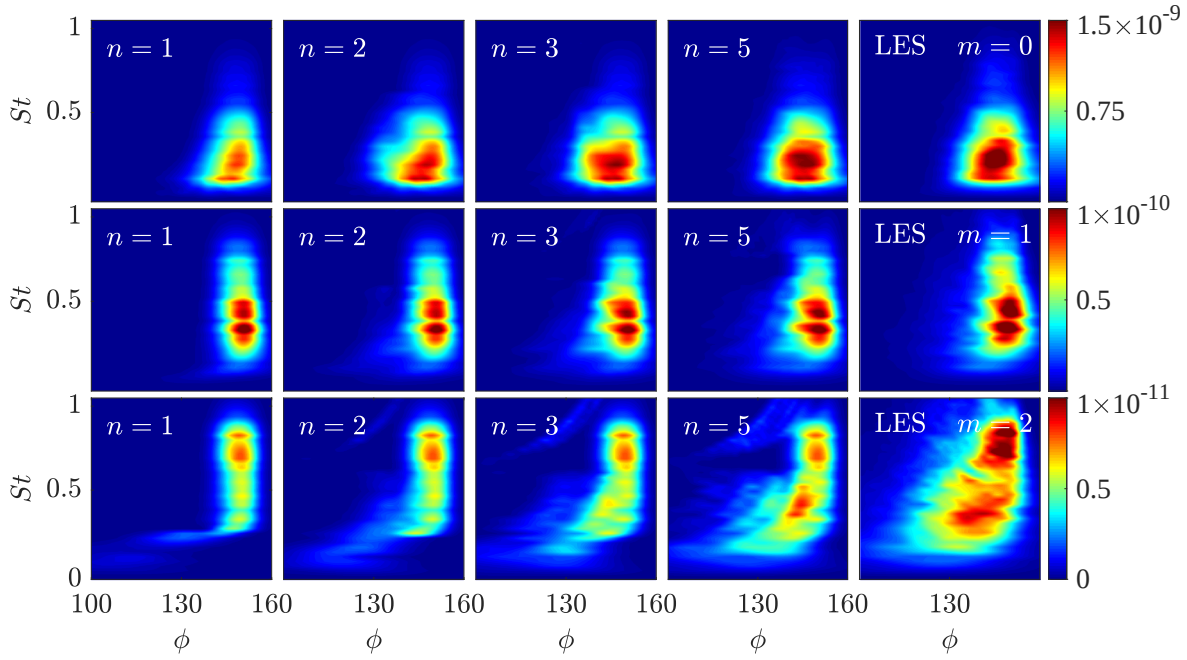

FIG. 11. PSD of far-field from propagating the LES pressure fluctuations of the $M_j = 1.5$ jet at radial surface $r/D = 6$ from $St = [0, 1]$ and $x/D = [0, 30]$ via the Kirchhoff surface to $\rho/D = 100$ for three azimuthal wavenumbers, $m = [0, 2]$. The right most column presents the LES values and the contour levels associated with each row.

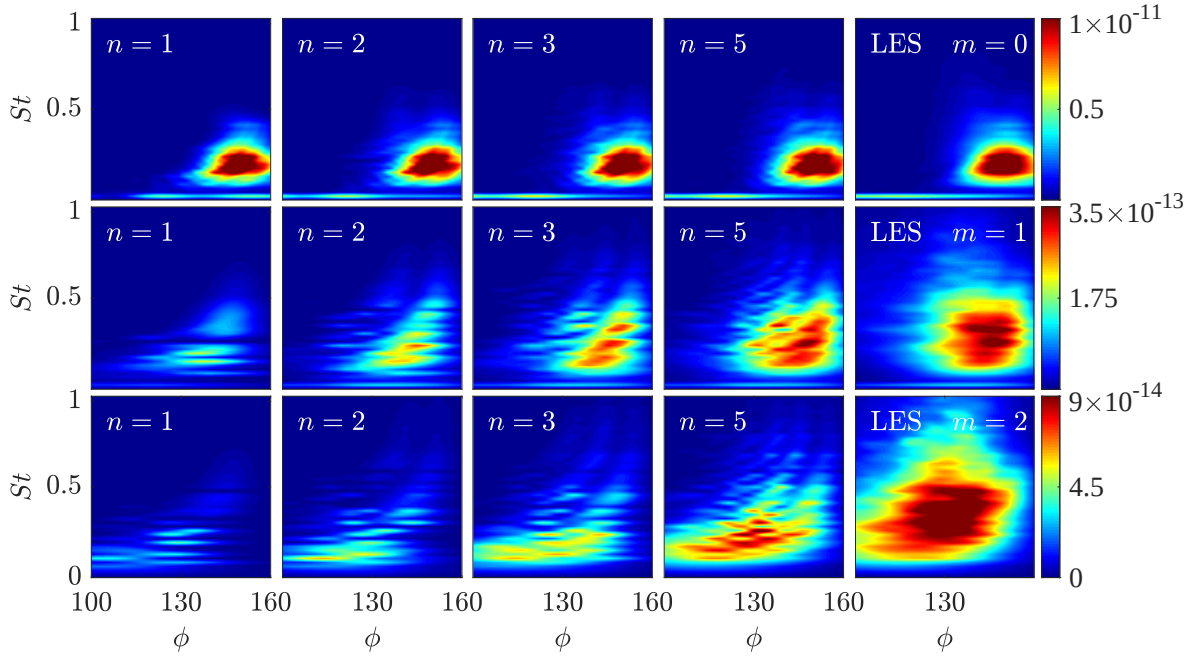

FIG. 12. PSD of far-field from propagating the LES pressure fluctuations of the $M_j = 0.9$ jet at radial surface $r/D = 6$ from $St = [0, 1]$ and $x/D = [0, 30]$ via the Kirchhoff surface to $\rho/D = 100$ for three azimuthal wavenumbers, $m = [0, 2]$. The right most column presents the LES values and the contour levels associated with each row.

possesses the lowest uncertainty. These values for the two jets and three azimuthal wavenumbers are shown in figure 13. For the $M_j = 1.5$ jet, we see that the forcing amplitudes for $m = 0$ and $m = 1$ fall upon lines of constant slope for the most acoustically significant frequency ranges, $St = 0.1 - 0.8$. The $m = 2$ data similarly collapse to a line of constant slope, however, the trend is not as clear. Similar observations also hold for the $M_j = 0.9$ jet. We also stress that these curves depend on both the data and the resolvent gains, Σ. Including the gains is crucial to collapsing the observed trends.

We now look to fit the data with simple curves of the form,

$$\tilde{\lambda}_{m,\omega} = a_m St^{b_m}. \tag{31}$$

For the nonzero azimuthal wavenumbers, the data represent the sum of both the clockwise (m) and counter-clockwise ($-m$) directions about the round jet, such that a_m represents $a_{+m} + a_{-m}$, or $2a_{+m}$, since $a_{+m} \approx a_{-m}$, as either rotation about the jet is of equal probability. The exponent, b_m is unaffected by this symmetry. Figure 13 provides the lines of best fit, where the fits are computed over the acoustically relevant region of $St = 0.13 - 0.7$ for the $M_j = 1.5$ and $St = 0.22 - 1$ for the $M_j = 0.9$. We find the difference in the frequency ranges by adjusting the Strouhal number by Mach number, $St_{0.9} = St_{1.5} \times 1.5/0.9$, meaning each range is associated with the same range of acoustic Strouhal number, St_{c_∞}. The upper bound for the $M_j = 0.9$ case extends to $St = 1.17$, however, we cap the upper bound to $St = 1$ as done throughout this manuscript.

Table I provides the fit coefficients for each jet and azimuthal wavenumber. At present, we do not have any physical interpretations of these fits, other than the obvious fact that the power law gives an expected decrease in energy as frequency increases (and thus the length scales of the structures decrease). We suspect we may find similar curves via projection of the resolvent forcing modes with the turbulent kinetic energy or other mean-flow quantities, but leave this for future work.

To determine how well such curves predict the data, we use the fitted curves to compute,

$$\tilde{\boldsymbol{S}}_{yy}(\phi) = \tilde{\lambda}_{m,\omega} \tilde{\boldsymbol{U}} \Sigma^2 \tilde{\boldsymbol{U}}^*, \tag{32}$$

where $\tilde{\boldsymbol{U}}$ represents the truncated resolvent basis to rank-n. Additionally, as the low-frequency regions are not acoustically important, nor can we expect our methods to have accurately captured such large structures in the finite domain used, we use the piece-wise function

$$\tilde{\lambda}_{m,\omega} = a_m St^{b_m} \quad \text{for} \quad St > St_{min} \tag{33}$$

$$\tilde{\lambda}_{m,\omega} = a_m St_{min}^{b_m} \quad \text{for} \quad St \leq St_{min}, \tag{34}$$

where $St_{min} = 0.13$ and 0.22 for $M_j = 1.5$ and $M_j = 0.9$, respectively. Figure 14 and 15 present the predicted PSD using $n = [1, 2, 3, 5]$ modes for the three azimuthal wavenumbers and two turbulent jets. For the $M_j = 1.5$ jet, the rank-1 model yields a close approximation of the reconstructions of figure 11. The same is observed for the $M_j = 0.9$ case, except for $m = 2$ which does not agree at low frequencies; however, we suspect such frequencies to be inaccurate for the domain used.

Proceeding to the higher mode predictions of the $M_j = 1.5$ jet we see little difference, particularly at the loudest regions of the PSD plots, with increases only seen at smaller angles. This lack of change from the rank-1 prediction shows that the forcing amplitude is underpredicted for resolvent modes $n > 1$ by the model, meaning that the actual forcing is greater than $\tilde{\lambda}_{m,\omega}\sigma_n^2$ for $n > 1$. Physically, this observation aligns with differences found between the forcing energy of two mechanisms in turbulent jets, the KH and Orr mechanisms (Pickering *et al.*, 2020b). The KH dominates the optimal resolvent modes at the azimuthal wavenumbers and frequencies considered here, however, a family of Orr-type modes dominate the $n > 1$ region of the spectrum. The main consequence of this for the present work is the distinct change in the spatial location of the associated forcing modes. For KH modes, the forcing mode is found localized near the nozzle, while forcing modes associated with the Orr-mechanism are located downstream where the turbulence is significantly more energetic (Pickering *et al.*, 2020a; Schmidt *et al.*, 2018). Thus, this difference necessitates knowledge of the relative magnitudes associated with each forcing mechanism. In the simple approach taken here, it would require a calibration of $n = 2$, however, the uncertainty in such a fit increases drastically, and due to the rather close fits of the rank-1 model, we leave this topic for future work and continue with the rank-1 model.

An analogous difficulty with $n > 1$ is also observed for the $M_j = 0.9$ jet. For $m = 0$, the forcing of the sub-optimal, Orr-type modes is over predicted, contrary to the under prediction for the $M_j = 1.5$ jet. This could result from the acoustic efficiency of the KH mechanism decreasing with Mach number, while the Orr-type modes maintain their ubiquitous presence in the turbulent jet. Such a finding underscores the necessity to determine a forcing model that represents both KH and Orr modes, as their relative energies differ amongst varied flow conditions.

With the rank-1 prediction in hand, we conclude by computing the overall sound pressure level (OASPL). Figure 16 presents multiple calculations of the OASPL from both jets. For the $M_j = 1.5$ case, data from a FW-H surface coupled directly with the LES simulation is available (similar data for the $M_j = 0.9$ case is not available) for comparison and the black lines represent this LES data, with the solid line denoting the total OASPL at $100D$ from the nozzle, while the dashed line gives the contributions from only the $m = 0$ component. The latter component is what we wish to compare for the remainder of the paper for two reasons. First, the difference between the total and $m = 0$ FW-H OASPLs is 2dB at peak noise from $\phi = 130° - 160°$. Second, the previous reconstructions and model show that the higher azimuthal wavenumbers require multiple modes to be ac-

	$M_j = 1.5$			$M_j = 0.9$		
Param.	$m = 0$	$m = 1$	$m = 2$	$m = 0$	$m = 1$	$m = 2$
a_m	7.10×10^{-10}	3.89×10^{-10}	4.66×10^{-10}	2.65×10^{-11}	1.38×10^{-11}	6.14×10^{-12}
b_m	-2.58	-1.7	-1.76	-5.80	-3.77	-3.13

TABLE I. Fit parameters used for the $M_j = 1.5$ and $M_j = 0.9$ jets shown in figure 13.

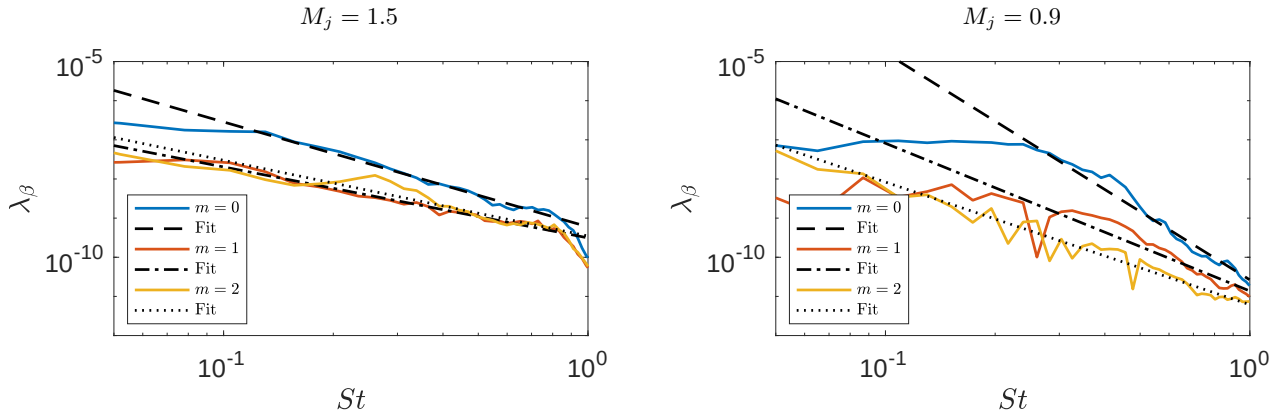

FIG. 13. Values of the reconstruction projection coefficient, λ_β, of the first resolvent mode for the azimuthal wavenumbers $m = 0 - 2$ and their associated fits, the parameters of which are provided in table I.

curate. Thus, we only compare the $m = 0$ component as it both represents most of the peak acoustic energy and may be reasonably represented at rank-1.

The blue lines in figure 16 represent approximations of the KS surface and the resolvent model for both jets. Comparisons of the $m = 0$ component for the $M_j = 1.5$ jet show the KS surface consistently over predicting the FW-H values by 2dB. The rank-1, $m = 0$ resolvent model, trained on the KS surface, which alternatively could have been trained of the FW-H data, aligns fairly well with the KS curve at the loudest angles. The greatest difference is that the resolvent model peaks at an angle of about 5 degrees higher than the LES data. Interestingly, a similar experiment and simulation in Brès *et al.* (2017) disagreed by the same angle. Although $100D$ data from the experiment is not available, projecting the resolvent modes onto this data would likely result in better alignment, as shifting the LES data by 5 degrees results in a significantly improved estimate. However, as the ultimate source of the discrepancy is unknown, we avoid making any corrections to the model based on these observations.

We see similar behavior between the KS surface and the resolvent model for the transonic case. The dashed line in figure 16 represents the total OASPL found via the KS surfaces and the $m = 0$ only OASPL shows a minor difference of 0.5dB at peak angles. The rank-1 $m = 0$ resolvent model again presents agreement of the peak OASPL to within 2dB. We stress that this result for the $M_j = 0.9$ jet is rather surprising as many previous studies, although computed in the near-field, found the acoustic field required many modes to agree within 2dB (Freund and Colonius, 2009; Towne *et al.*, 2015). This shows that the eddy-viscosity model included in our resolvent analysis significantly reduces the rank of the acoustic jet problem. Further, we note that this transonic jet has been extensively verified by experimental data in the near-field and at $\rho = 50D$, and, although we extend the results to $100D$, the peak angles of the KS and the resolvent model are closely aligned when compared to the $M_j = 1.5$ case.

IV. CONCLUSIONS

We formulated resolvent analysis to serve as an acoustic analogy by relating the near-field resolvent forcing to both the near- and far-field acoustic regions. Leveraging the availability of an LES database, we examined resolvent-based reconstructions of the acoustic PSD for turbulent $M_j = 1.5$ and $M_j = 0.9$ jets. We represented the forcing cross-spectral density matrix with a truncated set of resolvent modes and approximated the amplitudes of the modes with best-fit expansion coefficients of realizations from the LES acoustic field. We found that models comprising of just a single resolvent mode can accurately reconstruct the acoustic field for the first two azimuthal modes for a $M_j = 1.5$ jet and the $m = 0$ azimuthal mode for the $M_j = 0.9$ jet. To reconstruct higher azimuthal modes, the resolvent basis must be increased to at least 5 modes (i.e. $m = 2$ and $m = 1, 2$ for $M_j = 1.5$ and $M_j = 0.9$, respectively). In both jets, the use of an eddy-viscosity model in the resol-

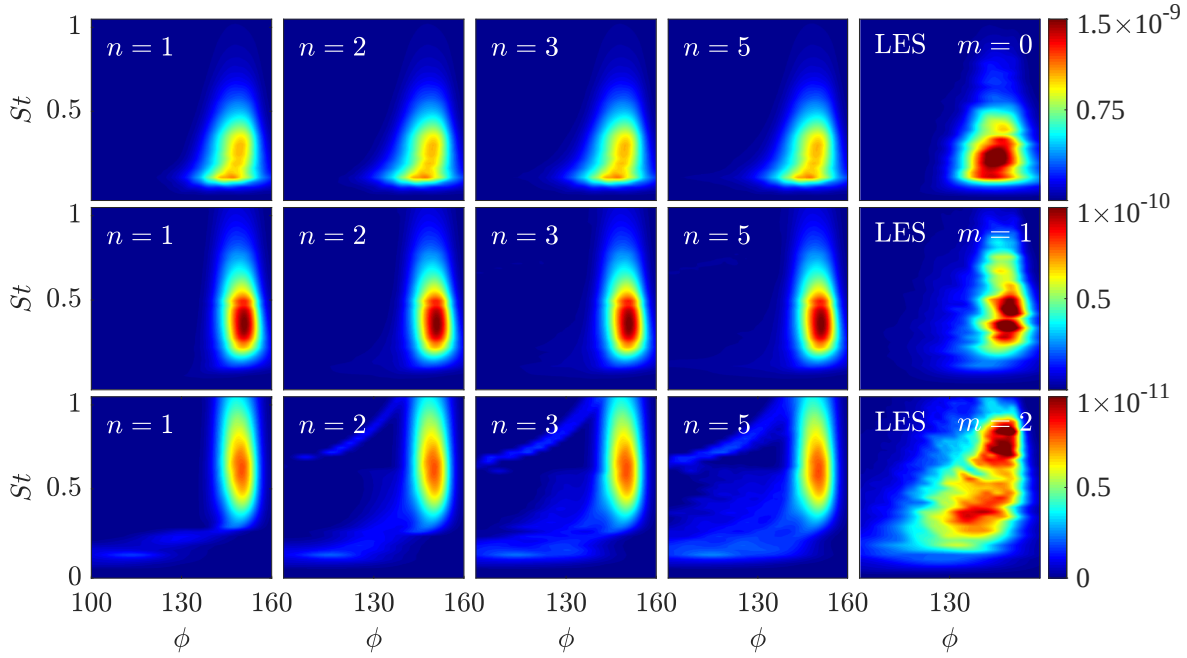

FIG. 14. PSD of the simple resolvent model of the $M_j = 1.5$ jet. The presentation mirrors that of figure 11.

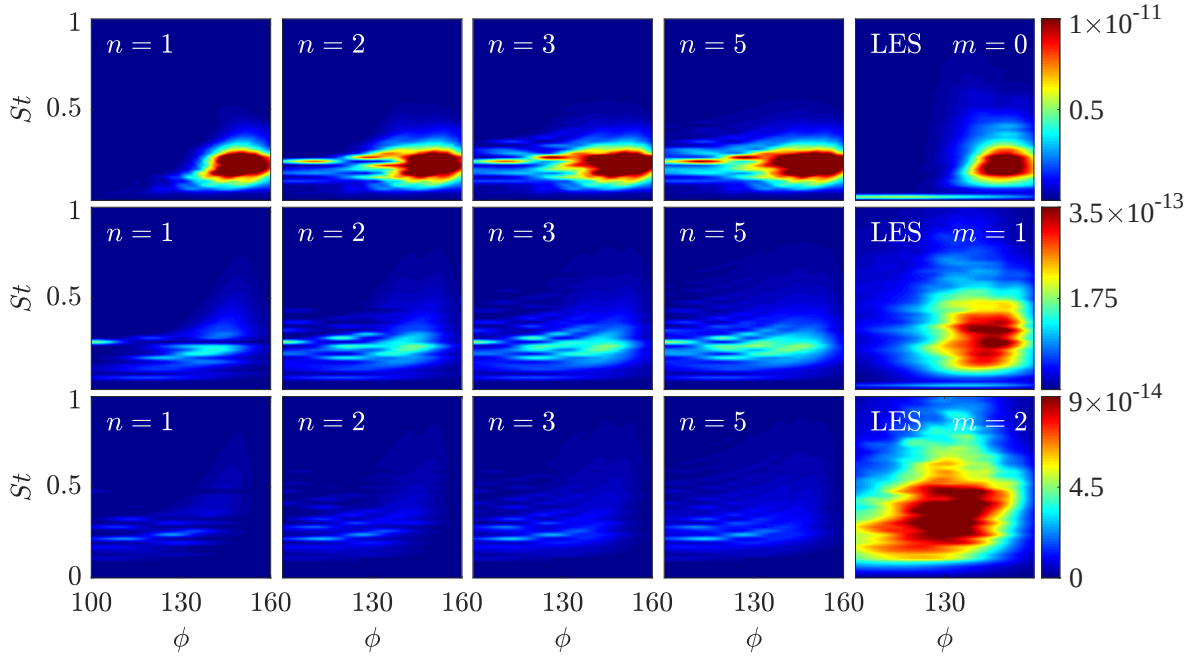

FIG. 15. PSD of the simple resolvent model of the $M_j = 0.9$ jet. The presentation mirrors that of figure 12.

vent formulation led to clearly superior results compared to a fixed turbulent Reynolds number.

Based on the ability of the rank-1 reconstructions to describe the PSD, we investigated a simple model to collapse the forcing coefficients to one scaling function per azimuthal wavenumber (and Mach number). We found that a power law representation, with only a scaling and an exponent, suffices to model the coefficient of the optimal resolvent mode. Fortunately, the first resolvent mode contains much of the acoustic energy, and reductions of

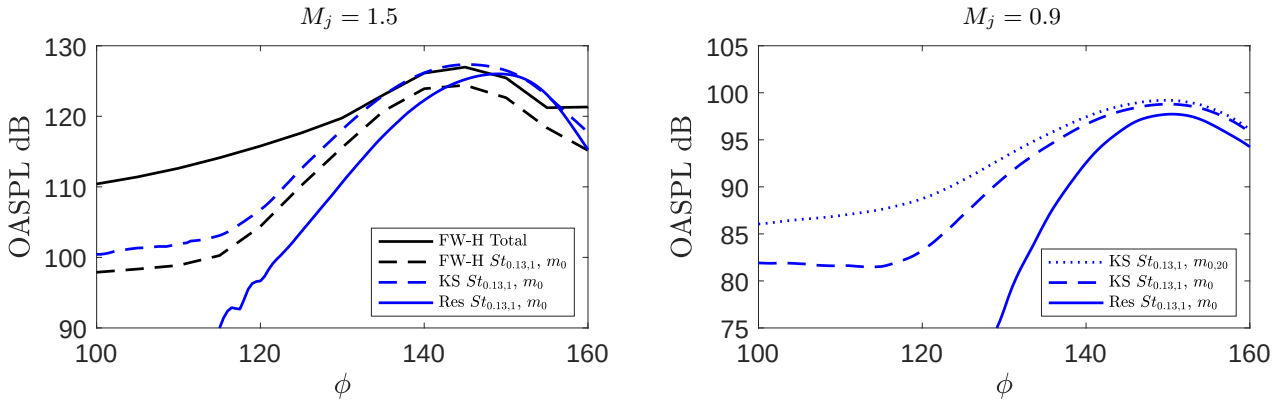

FIG. 16. OASPL of the $M_j = 1.5$ (left) and $M_j = 0.9$ (right) turbulent jets at $100D$ from the nozzle over the arc ϕ. The solid black line denotes the total OASPL from the FW-H surface of the LES, while the dashed black line presents the contribution to the OASPL from only azimuthal wavenumber $m = 0$. Blue lines represent approximations, where the dotted line is the KS considering 20 azimuthal modes over $St = 0.1 - 1$, the dashed line considers only $m = 0$, and the solid line gives the $m = 0$ resolvent estimation.

the gain for this specific mode (related to the KH mechanism) are likely to provide the greatest reductions in the peak noise of the acoustic field. However, the model does not accurately account for the suboptimal modes, under predicting their role in the $M_j = 1.5$ jet and over predicting them for the $M_j = 0.9$ jet (for at least the $m = 0$ azimuthal wavenumber).

Regardless of this difficulty, the rank-1 $m = 0$ resolvent models estimate the peak noise to within 2dB for both the $M_j = 1.5$ and $M_j = 0.9$ jets. Further, the ability of the resolvent basis to describe much of the acoustic field with only a handful of modes across multiple Mach numbers, a large range of frequencies, and the acoustically dominant azimuthal wavenumbers is promising. This shows that the resolvent framework already contains the appropriate acoustic functions to describe jet noise. In future work, we will seek a fully predictive model by estimating the forcing coefficients from mean flow quantities available from RANS.

ACKNOWLEDGMENTS

The authors would like to thank André Cavalieri, Oliver Schmidt, and Georgios Rigas for many productive discussions on topics related to this paper. This research was supported by a grant from the Office of Naval Research (grants No. N00014- 16-1-2445 and N00014-20-1-2311) with Dr. Steven Martens as program manager. E.P. was supported by the Department of Defense (DoD) through the National Defense Science & Engineering Graduate Fellowship (NDSEG) Program. P.J. acknowledges funding from the Clean Sky 2 Joint Undertaking (JU) under the European Union's Horizon 2020 research and innovation programme under grant agreement No 785303. Results reflect only the authors' views and the JU is not responsible for any use that may be made of the information it contains. The LES study was performed at Cascade Technologies, with support from ONR and NAVAIR SBIR project, under the supervision of Dr. John T. Spyropoulos. The main LES calculations were carried out on DoD HPC systems in ERDC DSRC.

APPENDIX A: KIRCHHOFF SURFACE DERIVATION

We begin with the homogeneous wave equation:

$$\frac{\partial^2 p'}{\partial t^2} - \nabla^2 p' = 0, \tag{A1}$$

where p' is a function of x, r, θ, t and can be expressed, due to stationarity in time, homogeneity in the azimuthal direction, and an imposed periodicity in the streamwise direction, as $p'(x, r, \theta, t) = \hat{p}(r)e^{-i\omega t + -im\theta - ikx}$. Applying this definition of the pressure, the wave equation gives

$$\frac{\partial^2 \hat{p}}{\partial r^2} + \frac{1}{r}\frac{\partial \hat{p}}{\partial r} + \left(\omega^2 - \frac{m^2}{r^2} - k^2\right)\hat{p} = 0. \tag{A2}$$

The general solution of (A2) is

$$\hat{p}_m(r, k, \omega) = c_1 J_m(\sqrt{\omega^2 - k^2}r) + c_2 Y_m(\sqrt{\omega^2 - k^2}r), \tag{A3}$$

where J_m and Y_m are Bessel functions of the first and second kind, respectively, and satisfying the Sommerfeld radiation condition reduces the expression to

$$\hat{p}_m(r, k, \omega) = c(k, \omega)H_m(\sqrt{\omega^2 - k^2}r), \tag{A4}$$

where H_m is the Hankel function of the first kind. We can then solve for the unknown coefficients by using the surface at the edge of the boundary, $r = R$

$$c(k, \omega) = \hat{p}_m(R, k, \omega)/H_m(\sqrt{\omega^2 - k^2}R). \tag{A5}$$

Therefore the particular solution is (as reported by Freund (2001)),

$$\hat{p}_m(r,k,\omega) = \hat{p}_m(R,k,\omega)H_m(\sqrt{\omega^2-k^2}r)/H_m(\sqrt{\omega^2-k^2}R). \tag{A6}$$

APPENDIX B: GOVERNING EQUATIONS

Conservation of mass, momentum, and energy for a compressible, Newtonian fluid are written as,

$$\frac{D\rho}{Dt} = -\rho\Theta, \tag{B1}$$

$$\rho\frac{D\boldsymbol{u}}{Dt} = -\frac{1}{\gamma M_j^2}\nabla(\rho T) + \nabla\cdot\left[\mu\left((\nabla\boldsymbol{u}) + (\nabla\boldsymbol{u})^T - \frac{2}{3}\Theta\mathbb{I}\right)\right], \tag{B2}$$

$$\rho\frac{DT}{Dt} = -\frac{1}{\gamma M_j^2}\rho T\Theta + \frac{\mu}{(\gamma-1)M_j^2 Pr_\infty}\nabla^2 T + \gamma M_j^2\mu \left[\frac{1}{2}\left\{(\nabla\boldsymbol{u}) + (\nabla\boldsymbol{u})^T\right\} : \left\{(\nabla\boldsymbol{u}) + (\nabla\boldsymbol{u})^T\right\} - \frac{2}{3}\Theta^2\right], \tag{B3}$$

respectively, where $\Theta = \nabla\cdot\boldsymbol{u}$ is the dilatation. We take $Pr_\infty = 0.7$ and $\gamma = 1.4$ as constants. The equations have been made nondimensional with the jet density (ρ_j), speed (U_j) , and diameter, D. The nondimensional viscosity, $\mu = \frac{1}{Re_j}$, is also a constant.

Applying the Reynolds decomposition (i.e. $\boldsymbol{q}(\boldsymbol{x},t) = \bar{\boldsymbol{q}}(\boldsymbol{x}) + \boldsymbol{q}'(\boldsymbol{x},t)$) to the above equations and separating terms that are linear and nonlinear in the fluctuations to the left- and right-hand sides, respectively, gives

$$\frac{\bar{D}\rho'}{Dt} + \boldsymbol{u}'\cdot\nabla\bar{\rho} + \rho'\bar{\Theta} + \bar{\rho}\Theta' = f_\rho, \tag{B4}$$

$$\bar{\rho}\frac{\bar{D}\boldsymbol{u}'}{Dt} + \bar{\rho}\boldsymbol{u}'\cdot\nabla\overline{\boldsymbol{u}} + \rho'\overline{\boldsymbol{u}}\cdot\nabla\overline{\boldsymbol{u}} + \frac{1}{\gamma M_j^2}\left(\bar{\rho}\nabla T' + \rho'\nabla\bar{T} + \bar{T}\nabla\rho' + T'\nabla\bar{\rho}\right) - \nabla\cdot\left[\mu\left((\nabla\boldsymbol{u}') + (\nabla\boldsymbol{u}')^T - \frac{2}{3}\Theta'\mathbb{I}\right)\right] = \boldsymbol{f_u}, \tag{B5}$$

$$\bar{\rho}\frac{\bar{D}T'}{Dt}\bar{\rho}\mathbf{u}'\cdot\nabla\bar{T} + \frac{1}{\gamma M_j^2}\left(\bar{T}\Theta' + T'\bar{\Theta}\right) + \rho'\{\overline{\mathbf{u}}\cdot\nabla\bar{T} + \frac{\bar{\rho}}{\gamma M_j^2}\bar{T}\bar{\Theta}\} - \frac{\mu}{(\gamma-1)M_j^2 Pr_\infty}\nabla^2 T' - \gamma M_j^2\mu \left[\left\{(\nabla\overline{\mathbf{u}}) + (\nabla\overline{\mathbf{u}})^{\mathrm{T}}\right\} : \left\{(\nabla\mathbf{u}') + (\nabla\mathbf{u}')^{\mathrm{T}}\right\} - \frac{4}{3}\bar{\Theta}\Theta'\right] = f_T. \tag{B6}$$

with $\frac{\bar{D}}{Dt} = \frac{\partial}{\partial t} + \overline{\boldsymbol{u}}\cdot\nabla$, and where we have grouped all the nonlinear terms as forcing terms on the right-hand-sides.

The left-hand-side is then transformed to a cylindrical coordinate frame and Fourier transformed in time (ω) and azimuth (m). The resulting equations are discretized as discussed in Schmidt *et al.* (2018).

For inclusion of the RANS eddy-viscosity model, we replace μ in equations (B4) to (B6) with $\mu + \mu_T$.

Brès, G. A., Bose, S. T., Emory, M., Ham, F. E., Schmidt, O. T., Rigas, G., and Colonius, T. (**2018**). "Large eddy simulations of co-annular turbulent jet using a voronoi-based mesh generation framework" AIAA Paper 2018-3302.

Brès, G. A., Ham, F. E., Nichols, J. W., and Lele, S. K. (**2017**). "Unstructured large-eddy simulations of supersonic jets," AIAA J. **55**(4), 1164–1184.

Brès, G. A., Jordan, P., Jaunet, V., Le Rallic, M., Cavalieri, A. V. G., Towne, A., Lele, S. K., Colonius, T., and Schmidt, O. T. (**2018**). "Importance of the nozzle-exit boundary-layer state in subsonic turbulent jets," J. Fluid Mech. **851**, 83–124.

Cavalieri, A. V. G., Jordan, P., Agarwal, A., and Gervais, Y. (**2011**). "Jittering wave-packet models for subsonic jet noise," Journal of Sound and Vibration **330**(18-19), 4474–4492.

Cavalieri, A. V. G., Jordan, P., and Lesshafft, L. (**2019**). "Wave-packet models for jet dynamics and sound radiation," Appl. Mech. Rev. **71**(2), 020802.

Chu, B.-T. (**1965**). "On the energy transfer to small disturbances in fluid flow (Part I)," Acta Mechanica **1**(3), 215–234.

Crighton, D. G., and Gaster, M. (**1976**). "Stability of slowly diverging jet flow," J. Fluid Mech. **77**(2), 397–413.

Crow, S. C., and Champagne, F. H. (**1971**). "Orderly structure in jet turbulence," J. Fluid Mech. **48**(3), 547–591.

Freund, J. B. (**2001**). "Noise sources in a low-Reynolds-number turbulent jet at Mach 0.9," J. Fluid Mech. **438**, 277.

Freund, J. B., and Colonius, T. (**2009**). "Turbulence and sound-field POD analysis of a turbulent jet," Int. J. Aeroacoust. **8**(4), 337–354.

Goldstein, M. E. (**2003**). "A generalized acoustic analogy," J. Fluid Mech. **488**, 315–333.

Hwang, Y., and Cossu, C. (**2010**). "Amplification of coherent streaks in the turbulent couette flow: an input–output analysis at low Reynolds number," J. Fluid Mech. **643**, 333–348.

Jeun, J., and Nichols, J. W. (**2018**). "Input-output analysis of Mach 0.9 jet noise," arXiv preprint arXiv:1806.09280 .

Jeun, J., Nichols, J. W., and Jovanović, M. R. (**2016**). "Input-output analysis of high-speed axisymmetric isothermal jet noise," Phys. Fluids **28**(4), 047101.

Jordan, P., and Colonius, T. (**2013**). "Wave packets and turbulent jet noise," Annu. Rev. Fluid Mech. **45**, 173–195.

Jovanović, M. R. (**2021**). "From bypass transition to flow control and data-driven turbulence modeling: An input–output viewpoint," Ann. Rev. Fluid Mech. **53**(1), null, doi: 10.1146/annurev-fluid-010719-060244.

Juve, D., Sunyach, M., and Comte-Bellot, G. (**1979**). "Filtered azimuthal correlations in the acoustic far field of a subsonic jet," AIAA J. **17**(1), 112–113.

Lesshafft, L., Semeraro, O., Jaunet, V., Cavalieri, A. V. G., and Jordan, P. (**2019**). "Resolvent-based modelling of coherent wavepackets in a turbulent jet," Phys. Rev. Fluids **4**(6), 063901.

Lighthill, M. J. (**1952**). "On sound generated aerodynamically i. general theory," Proc. R. Soc. Lond. A **211**(1107), 564–587.

McKeon, B. J., and Sharma, A. S. (**2010**). "A critical-layer framework for turbulent pipe flow," J. Fluid Mech. **658**, 336–382.

Michalke, A. (**1977**). "Instability of a compressible circular free jet with consideration of the influence of the jet boundary layer thickness," .

Mollo-Christensen, E. (**1967**). "Jet noise and shear flow instability seen from an experimenter's viewpoint," J. Appl. Mech. **34**, 1–7.

Morra, P., Semeraro, O., Henningson, D. S., and Cossu, C. (**2019**). "On the relevance of Reynolds stresses in resolvent analyses of turbulent wall-bounded flows," J. Fluid Mech. **867**, 969–984.

Papamoschou, D. (**2018**). "Wavepacket modeling of the jet noise source," Int. J. of Aeroacoust. **17**(1-2), 52–69.

Pickering, E., Rigas, G., Nogueira, P. A. S., Cavalieri, A. V. G., Schmidt, O. T., and Colonius, T. (**2020**a). "Lift-up, kelvin–helmholtz and orr mechanisms in turbulent jets," J. Fluid Mech. **896**, A2, doi: 10.1017/jfm.2020.301.

Pickering, E., Rigas, G., Schmidt, O. T., Sipp, D., and Colonius, T. (**2020**b). "Optimal eddy viscosity for resolvent-based models of coherent structures in turbulent jets," arXiv preprint arXiv:2005.10964 https://arxiv.org/abs/2005.10964.

Pickering, E., Rigas, G., Sipp, D., Schmidt, O. T., and Colonius, T. (**2019**). "Eddy viscosity for resolvent-based jet noise models," in *25th AIAA/CEAS Aeroacoustics Conference*, p. 2454, doi: 10.2514/6.2019-2454.

Schlinker, R. H., Simonich, J. C., Reba, R. A., Colonius, T., Gudmundsson, K., and Ladeinde, F. (**2009**). "Supersonic jet noise from round and chevron nozzles: Experimental studies" AIAA Paper 2009-3257.

Schlinker, R. H., Simonich, J. C., Reba, R. A., Colonius, T., and Ladeinde, F. (**2008**). "Decomposition of high speed jet noise: Source characteristics and propagation effects" AIAA Paper 2008-2890.

Schmidt, O. T., Towne, A., Rigas, G., Colonius, T., and Brès, G. A. (**2018**). "Spectral analysis of jet turbulence," J. Fluid Mech. **855**, 953–982.

Sinha, A., Rodríguez, D., Brès, G. A., and Colonius, T. (**2014**). "Wavepacket models for supersonic jet noise," J. Fluid Mech. **742**, 71–95.

Towne, A., Bres, G. A., and Lele, S. K. (**2017**). "A statistical jet-noise model based on the resolvent framework," in *23rd AIAA/CEAS Aeroacoustics Conference*, p. 3706.

Towne, A., Colonius, T., Jordan, P., Cavalieri, A. V., and Bres, G. A. (**2015**). "Stochastic and nonlinear forcing of wavepackets in a Mach 0.9 jet," in *21st AIAA/CEAS Aeroacoustics Conference*, p. 2217.

Towne, A., Lozano-Durán, A., and Yang, X. (**2020**). "Resolvent-based estimation of space–time flow statistics," J. Fluid Mech. **883**.

Towne, A., Schmidt, O. T., and Colonius, T. (**2018**). "Spectral proper orthogonal decomposition and its relationship to dynamic mode decomposition and resolvent analysis," J. Fluid Mech. **847**, 821–867.

Zare, A., Jovanović, M. R., and Georgiou, T. T. (**2017**). "Colour of turbulence," J. Fluid Mech. **812**, 636–680.